NAVAL POSTGRADUATE SCHOOL
Monterey, California

THESIS

THE EFFECTS OF TITANIUM ON THE MECHANICAL PROPERTIES OF SHIELDED METAL ARC WELDING (SMAW) OF C-MN STEELS

by
Michael K. Greene

March, 1997

Thesis Advisor: Alan G. Fox

Approved for public release; distribution is unlimited.

REPORT DOCUMENTATION PAGE

Form Approved OMB No. 0704-0188

1. AGENCY USE ONLY *(Leave blank)*	2. REPORT DATE	3. REPORT TYPE AND DATES COVERED
	March 1997	Master's Thesis

4. TITLE AND SUBTITLE
THE EFFECTS OF TITANIUM ON THE MECHANICAL PROPERTIES OF SHIELDED METAL ARC WELDING (SMAW) OF C-MN STEELS

5. FUNDING NUMBERS

6. AUTHOR(S)
Greene, Michael K.

7. PERFORMING ORGANIZATION NAME(S) AND ADDRESS(ES)
Naval Postgraduate School
Monterey, CA 93943-5000

8. PERFORMING ORGANIZATION REPORT NUMBER

9. SPONSORING / MONITORING AGENCY NAME(S) AND ADDRESS(ES)

10. SPONSORING / MONITORING AGENCY REPORT NUMBER

11. SUPPLEMENTARY NOTES
The views expressed in this thesis are those of the author and do not reflect the official policy or position of the Department of Defense or the U.S. Government.

12a. DISTRIBUTION / AVAILABILITY STATEMENT
Approved for public release; distribution unlimited.

12b. DISTRIBUTION CODE

13. ABSTRACT *(maximum 200 words)*

The strength and toughness of low alloy steel shielded metal arc weld (SMAW) metal is markedly improved by the presence of the microconstituent acicular ferrite. Since acicular ferrite is nucleated by the non-metallic inclusions present in the weld metal its presence is determined by the size, number, distribution and chemical composition of these inclusions. Previous work has shown that inclusions containing no titanium are usually ineffective as nucleants of acicular ferrite in some C-Mn steel weld metal whereas inclusions containing small amounts (less than 5%) of titanium or more can produce a microstructure containing as much as 70% of acicular ferrite.

14. SUBJECT TERMS	15. NUMBER OF PAGES
SMAW, C-Mn steel weldments, Non-Metalic Inclusions	108
	16. PRICE CODE

17. SECURITY CLASSIFICATION OF REPORT	18. SECURITY CLASSIFICATION OF THIS PAGE	19. SECURITY CLASSIFI- CATION OF ABSTRACT	20. LIMITATION OF ABSTRACT
Unclassified	Unclassified	Unclassified	UL

NSN 7540-01-280-5500 (Rev. 2-89)

Standard Form 298

Prescribed by ANSI

Std. 239-18

In the present work the size, number, distribution and chemistry of the inclusions in two C-Mn steel weld metals containing 1 and 28 ppm respectively of Ti were studied by scanning and transmission electron microscopy, energy dispersive x-ray (EDX) analysis and parallel electron energy loss spectroscopy (PEELS). This work showed that the inclusions in the 'Ti-free' sample contained rhodonite ($MnO.SiO_2$) sometimes complexed with copper sulfide (CuS). In the sample that contained 28 ppm Ti the nature of the inclusions was found to be far more complex, often containing three phases. However EDX and PEELS analyses indicated that the titanium adopts a valency of 4 and may be complexed as pyrophanite ($MnO.TiO_2$) and the presence of this compound seems to be responsible for the nucleation of acicular ferrite although the exact mechanism is not yet clear. This work shows that it is important to control the Ti content of steel weld metal so that strong tough microstructures are produced; this issue is obviously of critical importance in Naval ship construction.

Approved for public release; distribution is unlimited

THE EFFECTS OF TITANIUM ON THE MECHANICAL PROPERTIES OF SHIELDED METAL ARC WELDING (SMAW) OF C-MN STEELS

Michael K. Greene
Lieutenant, United States Navy
B.S., Auburn University, 1989

Submitted in partial fulfillment of the
requirements for the degree of

MASTER OF SCIENCE IN MECHANICAL ENGINEERING

from the

NAVAL POSTGRADUATE SCHOOL
March 1997

ABSTRACT

The strength and toughness of low alloy steel shielded metal arc weld (SMAW) metal is markedly improved by the presence of the microconstituent acicular ferrite. Since acicular ferrite is nucleated by the non-metallic inclusions present in the weld metal its presence is determined by the size, number, distribution and chemical composition of these inclusions. Previous work has shown that inclusions containing no titanium are usually ineffective as nucleants of acicular ferrite in some C-Mn steel weld metal whereas inclusions containing small amounts (less than 5%) of titanium or more can produce a microstructure containing as much as 70% of acicular ferrite.

In the present work the size, number, distribution and chemistry of the inclusions in two C-Mn steel weld metals containing 1 and 28 ppm respectively of Ti were studied by scanning and transmission electron microscopy, energy dispersive x-ray (EDX) analysis and parallel electron energy loss spectroscopy (PEELS). This work showed that the inclusions in the 'Ti-free' sample contained rhodonite ($MnO.SiO_2$) sometimes complexed with copper sulfide (CuS). In the sample that contained 28 ppm Ti the nature of the inclusions was found to be far more complex, often containing three phases. However EDX and PEELS analyses indicated that the titanium adopts a valency of 4 and may be complexed as pyrophanite ($MnO.TiO_2$) and the presence of this compound seems to be responsible for the nucleation of acicular ferrite although the exact mechanism is not yet clear. This work shows that it is important to control the Ti content of steel weld metal so that strong tough microstructures are produced; this issue is obviously of critical importance in Naval ship construction.

TABLE OF CONTENTS

I. INTRODUCTION

The U.S. Navy has stringent strength and toughness requirements for ship building steels and their weldments. Although, these are relatively easy to meet for base metal, as demonstrated by the successful use of HSLA and HY steels in ship construction the development of strong tough weld metals which can be used over a range of welding conditions (voltage, current, preheat/interpass temperature for particular applications) has proved much more difficult. An ideal weld metal would be one that could easily meet Navy strength and toughness requirements (for the grade of steel concerned) regardless of welding procedure.

In order to produce strong, tough steel weld metal the fusion zone microstructure must be carefully controlled. Use of the shielded metal arc (SMAW), submerged arc (SAW) and gas metal arc (GMA) welding methods on high strength steels can lead to complex microstructures which can include the following microconstituents: martensite, bainite, grain boundary ferrite, Widmanstatten ferrite and acicular ferrite. Weld metal microstructures which do not contain acicular ferrite can usually meet strength requirements but are often insufficiently tough unless the weldment is multi-run in which case tempered martensite and bainite can provide a tough microstructure. However, if acicular ferrite is present in the weld metal in significant amounts, then both the strength and toughness can be significantly improved. Consequently, the maximizing of the acicular ferrite in steel weld metal is an important issue for those engineers developing new weld wires for Navy use.

In order to generate steel weld metal that contains large amounts of acicular ferrite several conditions must be met. In the first place the weld metal carbon content and carbon equivalent must be such that its continuous cooling characteristics are appropriate for acicular ferrite formation. (This of course will be different for different welding procedures which have different heat inputs and efficiencies). Secondly the weld metal oxygen content must be at the correct level (usually in the range 200-400 ppm) so the non-metallic inclusions of appropriate size, number, distribution and chemistry are present, since these are responsible for the nucleation of acicular ferrite. This also implies that the level of deoxidizing elements (Mn, Si, Al, Ti, etc.) in the weld metal must also be carefully controlled.

Although it is well known that non-metallic inclusions are responsible for the nucleation of acicular ferrite in steel weld metal, there is only minimal understanding of the relationship between the chemistry and crystallography of the inclusions and the surrounding weld metal.

This is obviously a very important issue for those welding engineers who are trying to develop new weld filler wires for high strength steel applications. In the present work, attempts will be made to use transmission electron microscopy (TEM), energy dispersive x-ray (EDX) spectroscopy and parallel electron energy loss spectroscopy (PEELS) to understand the chemistry and crystallography of the inclusions which are responsible for the formation of acicular ferrite in submerged are weldments made on C-Mn steels.

II. BACKGROUND

A. HISTORY OF ACICULAR FERRITE

The term acicular ferrite was first proposed in 1930 by Davenport and Bain. From then on bainite and acicular ferrite were terms used interchangeably. It was not until the last 25 years that metallurgist have distinguished between intragranular nucleated acicular ferrite and the more common bainite which is nucleated on the grain boundaries of the prior austenite. Common bainite grows in a parallel plate-like structure. In contrast, acicular ferrite nucleates on inclusions, within grains, and develops platelets that arrange themselves in multiple directions. These acicular ferrite platelets are shorter because their growth is arrested by interaction with other platelets that grow from adjacent inclusions.

B. PROPERTIES

There is increasing interest in acicular ferrite because of its desirable effects on steel and steel weld metal. Acicular ferrite's plate-like structures arranged in multiple directions tend to both increase yield strength and fracture toughness. The yield strength is increased due to the displacive nature of the acicular ferrite transformation in which platelets grow in an invariant plane strain transformation [Ref. 10]. This strain transformation takes place at elevated temperatures when both the austenite and ferrite matrices are very accommodating. This "accommodation" leads to dislocation densities

that are quite large, of the order of $10^{14}/m^2$. These high dislocation densities provide increase in yield strength of up to 145 MPa [Ref. 10].

Fracture toughness is also enhanced in metals with high acicular ferrite concentrations because of the nature of crack propagation within a polycrystalline material. A crack going through a grain encounters numerous acicular ferrite platelets which are oriented in many different directions. Each platelet offers an increase in local distortion of the crystal lattice due to their high dislocation densities. Thus cracks require more energy to progress through the platelets and it is too difficult to follow the acicular ferrite interface. This impedes free crack motion and thus, increases the material's resistance to crack propagation and thus, its fracture toughness.

This beneficial structure of acicular ferrite tends to form a very fine array of interlocking platelets as shown in Figure (1). This optical micrograph was taken at a magnification of 630x at the centerline of a SMAW weld on a C-Mn steel at the captioned depth. A more in-depth discussion of this micrograph is provided in the Experimental section.

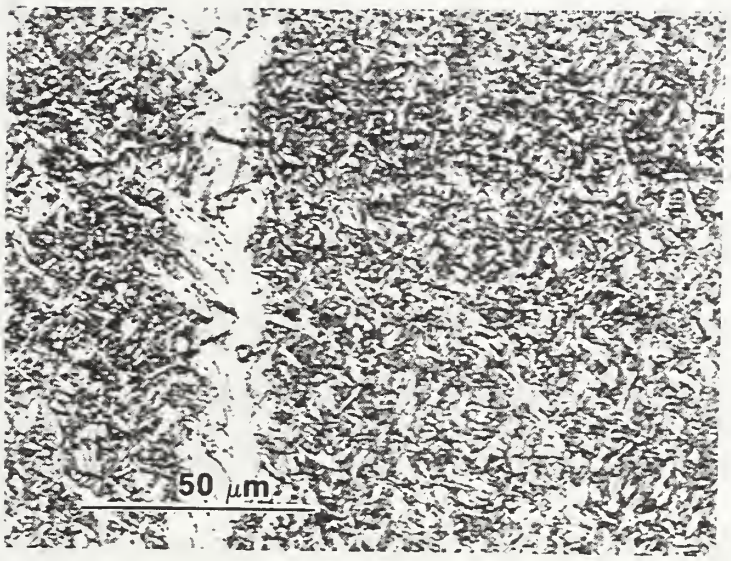

Figure 1 - Acicular ferrite with some Widmanstatten ferrite in a C-Mn weld metal.

C. REACTION MECHANISMS

There are four generally accepted mechanisms to explain why acicular ferrite may nucleate within an austenitic grain on non-metallic inclusions. The first and least complex is, simple heterogeneous nucleation. The second is epitaxial growth of the ferrite on a suitably oriented inclusion surface. The third mechanism is reduction of strain energy produced due to different thermal expansion coefficients between the matrix and inclusion. The last, and most complex of the four mechanisms arises from chemical effects in the matrix caused by local interactions with the inclusions. These various mechanisms are discussed in detail by Gregg et al. [Ref. 3].

1. Heterogeneous Nucleation

It is unlikely that simple heterogeneous nucleation of ferrite on an inclusion is the sole mechanism responsible for acicular ferrite. The first problem with this theory concerns the surface to volume energy associated with nucleation. Nucleation on an inclusion requires a larger surface angle than nucleation on the interior of a grain boundary. Thus more energy is required for ferrite to nucleate on an inclusion than on an austenite grain boundary. Secondly, Ricks et al. (1982) [Ref. 24], noted that ferrite should be more likely to nucleate on austenite to austenite interfaces than on the austenite to inclusion interfaces. This is because the surface energy for like compositions should be less than that of unlike compositions, namely ferrite-inclusion interfaces should require more energy than ferrite-austenite interfaces. Both of the aforementioned problems make simple nucleation of acicular ferrite on inclusions improbable.

2. Epitaxial Growth

The second mechanism is epitaxial growth of ferrite on a suitably oriented surface. This mechanism involves lattice matching where low index crystallographic planes of both ferrite and the inclusion have a similar spacing [Ref. 10]. The similarity of the structure and spacing reduce the energy required to cause nucleation. This nucleation on non-metallic inclusions has been directly observed by Grong et al. 1992 [Ref. 37]. Table (1) shows the disregistry between the various possible oxides which can make up the non-metallic inclusions and ferrite lattice. Note, that TiO has a relatively low disregistry on the plane of epitaxy in the Bain orientation which is when the {100} plane of the ferrite lattice

is parallel with the {100} plane of the inclusion and also that the <100> direction of the ferrite lattice is parallel with the <110> direction of the inclusion. The cube orientation referred to in Table (1) simply means that both the crystals of the inclusion and ferrite are in identical orientation.

Table 1 - List of inclusion misfit percentage with α–$Fe_{<110>}$ based on planar spacing reprinted from [Ref. 10].

Inclusion	Orientation	Plane of Epitaxy	Misfit %
TiO	Bain	{100}	3.0
TiN	Bain	{100}	4.6
γ - Alumina	Bain	{100}	3.2
Galaxite	Bain	{100}	1.8
CuS	Cube	{111}	2.8

3. Misfit Strain

The third mechanism is the reduction of strain energy produced due to different thermal expansion coefficients between the matrix and the inclusion. As the molten metal cools the first items to nucleate and solidify are the inclusions. The matrix solidifies much later. Since austenite and ceramic inclusions have a very different thermal expansion coefficient there is a strain field that is set up around each inclusion. Barrite and Edmonds

[Ref. 25] have suggested that such a strain field may be relieved by a transformation from austenite to ferrite. Table (2) provides thermal expansion coefficients for various weld metal inclusions. Austenite has been included for the purpose of comparison.

As noted by Gregg and Bhadeshia [Ref. 3] the thermal expansion coefficients for $MnO.Al_2O_3$, Al_2O_3 and TiO_2 are all similar, yet, they have significantly different efficiencies associated with their ability to nucleate acicular ferrite. For this reason, this mechanism alone, it is not likely to be solely responsible for acicular ferrite formation. But, misfit strain may still be a part of a complex transformation mechanism that depends on several interrelated mechanisms.

Table 2 - List of thermal expansion coefficients for various compounds reprinted from [Ref. 3].

Mineral	Coefficient of thermal expansion (α_T)	Temperature range measurement was taken (K)
$MnAl_2O_4$	$8.0x10^{-6}$	273 - 1073
Al_2O_3	$8.0x10^{-6}$	293 - 1853
TiO	$9.5x10^{-6}$	273 - 1050
TiN	$9.4x10^{-6}$	273 - 1073
MnS	$1.8x10^{-5}$	273 - 1073
Austenite	$2.3x10^{-5}$	N/A

4. Chemical Effects

The last mechanism commonly considered in the explanation of acicular ferrite nucleation is localized chemical effects associated with the steel next to the inclusions.

Gregg and Bhadeshia [Ref. 3] have conducted annealing experiments on steel/titanium oxide ceramic diffusion bonded interfaces at which energy dispersive x-ray analysis (EDX) shows local alloy depletion in the steel next to the steel/ceramic interface. They suggest, that, for TiO_2 and Ti_2O_3, oxygen reduction is occurring near the steel/ceramic interface such that, TiO is present at the interface. Yamamoto et al. 1993 [Ref. 26] also observed Ti_2O_3 reduction at the inclusion interface such that only TiO was left. These interactions which could also occur between Ti-containing inclusions and the local austenite matrix could reduce the local alloy concentrations of both Mn and Carbon in the steel around the inclusions. A reduction in these alloys would result in lower local hardenability and a greater likelihood that ferrite would be nucleated near the inclusion boundary.

The most probable mechanism for acicular ferrite nucleation at this time is a combination of epitaxial growth, reduction of strain energy and local chemical effects. Research to date has not been able to conclusively suggest any one of these three over another.

D. NON-METALLIC INCLUSIONS

1. General

Non-metallic inclusions are therefore the key to the nucleation of acicular ferrite. The size, shape distribution and composition of inclusions along with prior austenite grain size determine whether a steel will form acicular ferrite. Harrison and Farrar 1981 [Ref. 27] took a steel weld metal that had nucleated acicular ferrite, removed its inclusions and re-solidified it under exactly the same conditions. The metal would no longer nucleate

acicular ferrite. This experiment clearly shows that the inclusions, in Harrison and Farrar's experiment, were responsible for acicular ferrite nucleation.

Inclusions are formed by oxidation reactions within the metal alloy. Elements such as manganese (Mn), silicon (Si), titanium (Ti) and aluminum (Al) are used to kill or to remove oxygen from molten steel. This oxygen removal is essential to prevent porosity and its associated degraded mechanical properties. Once the alloy components react with oxygen they tend to rise to the surface of the molten metal. However, a significant number of these oxides are trapped inside the metal on solidification. Typically, weldments have of the order of 10^{18} oxide inclusions per cubic meter that are greater than 0.05 micron in diameter. The larger inclusions may be banded in solidification cell boundaries as noted by Sugden and Bhadeshia 1988 [Ref. 28].

Oxygen is thus an important element with respect to acicular ferrite formation. The concentration of oxygen along with steel Al, Mn and Si content will determine how much titanium will be present in the inclusions after the Al is consumed. Horii et al. (1986/1988), [Ref. 29] have proposed that oxygen reacts with aluminum then any excess oxygen reacts with titanium forming titanium oxides that are strong acicular ferrite initiators. Ringer et al. (1990), [Ref. 30] note that nitrogen in the molten metal can also react with Ti to form TiN before Ti oxides can be formed if the oxygen activity is low.

$$3O + 2Al \Rightarrow Al_2O_3 \quad (1)$$

$$xTi + yO \Rightarrow Ti_xO_y \quad (2)$$

where $x = 1, y = 1$ and $x = 2, y = 3$

$$x = 2,\ y = 3 \text{ and } x = 3,\ y = 5$$

The above oxidation states are all possible in titanium oxides.

$$Ti + N \Rightarrow TiN \qquad (3)$$

The natural progression of logic dictates that molten steels with both low nitrogen and Al concentrations should require a lower oxygen and Ti concentration to form the same amount of acicular ferrite. This conclusion was also reached by Bhadeshia [Ref. 10].

Inclusions in steels offer a two edged sword that steel designers and fabricators must appreciate. An appropriate inclusion density, size, distribution and chemistry may lead to the formation of acicular ferrite, a microconstituent responsible for good strength and toughness. High inclusion concentrations always pose the threat of void nucleation in ductile failure or cleavage sites in brittle fracture. A careful selection of material processing parameters such as cooling rate, oxygen concentration and deoxidants, such as Al and Ti, is very important. As steel strength increases, its sensitivity to non-metallic inclusions with respect to toughness will increase. A compromise must be made that provides the highest concentration of the desirable acicular ferrite platelets but keeps inclusion number and size distribution at an appropriate level.

It should be noted that the samples investigated in this paper contain a small concentration of boron (B), a known allotriomorphic ferrite poison. It may be argued that B may poison prior austenitic grain boundaries leaving only one nucleation path, acicular ferrite. Boron segregates to prior austenite grain boundaries and lowers their energies, thus making grain boundary and side plate ferrite less energetically feasible [Ref. 31].

Weld metals containing boron in concentrations of 50 ppm with several hundred ppm Ti have been noted to be very effective in nucleating acicular ferrite. In the present work the B content of the weld metals studied is less than 3 ppm and it is felt that this amount of boron is likely to have little effect on the nucleation of acicular ferrite.

2. Orientation of Acicular Ferrite with Respect to Prior Austenite

The orientation of inclusions within weld metal appears to be random as discussed by Dowling et al. (1986), [Ref. 13]. However, the orientation of acicular ferrite within the austenite matrix is not random. It is of the Kurdjimov-Sachs / Nishiyama-Wasserman (KS/NW) type. Thus the random inclusion must be oriented in a suitable relationship within the austenite matrix so that an acicular ferrite platelet can grow.

Grong et al. [Ref. 6] explored the random inclusion distribution that was mentioned earlier. For a single crystal inclusion they calculated that the probability that an inclusion lines up in a Bain orientation so that the KS/NW orientation is satisfied is 0.04. That is 4% of all single phase inclusions should provide suitable positions for acicular ferrite platelets to nucleate. Since most inclusions in steels are polycrystalline, Grong et al. suggested that the true probability that an inclusion lines up in a Bain region is at least 12%. As a result Grong et al. went on to estimate an upper limit to volume percent acicular ferrite, but they noted that this assumes only one nucleation per inclusion, which does not appear to be the case, see Figure (2). Nonetheless Grong et al. did approximately predict the correct size, shape and volume of the acicular ferrite platelets.

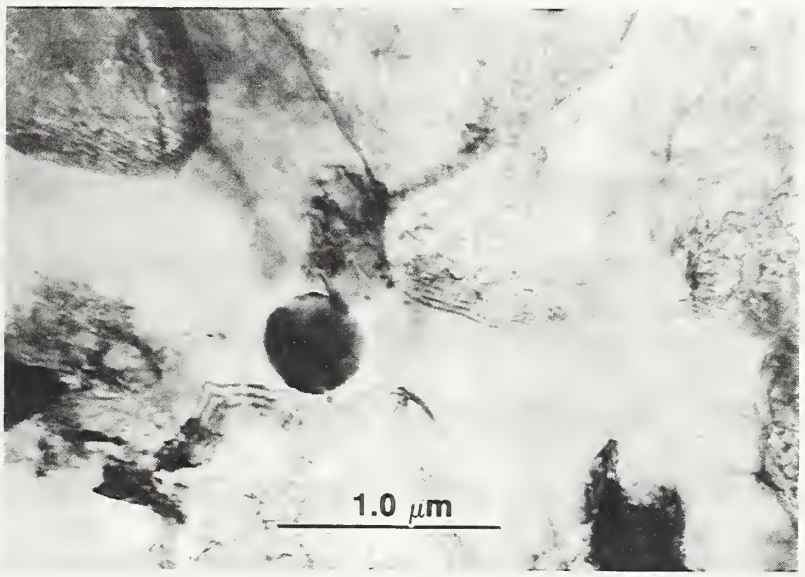

Figure 2 - Multiple nucleation of acicular ferrite on an inclusion in a C-Mn steel weld metal containing 28 ppm titanium.

E. NATURE OF INCLUSIONS BELIEVED TO FORM ACICULAR FERRITE

Inclusions in C-Mn steels are thought to be responsible for nucleation of acicular ferrite. To better understand the mechanism, by which the inclusions nucleate acicular ferrite a careful study of inclusion phases is in order.

Inclusions are primarily made up of oxides. Dowling et al. 1986 [Ref. 13] identified Mn, Al, and Ti oxides along with SiO_2 in aluminum killed low titanium steel weld metal. SiO_2 normally exists as a polycrystalline or even glassy structure [Ref. 32]. A

non-oxide inclusion that is often complexed with the oxide is MnS. Yamamoto et al. 1987 believed that MnS could be responsible for acicular ferrite. This has been disputed by Chijiiwa et al. [Ref. 18] and Abson [Ref. 16] who claim that MnS reduces acicular ferrite concentrations.

Dowling et al. [Ref. 13] note that in aluminum killed steel weld metal containing low levels of titanium, $MnO.Al_2O_3$ or galaxite may be responsible for nucleation of acicular ferrite. Babu et al. [Ref. 22] agree that galaxite may indeed nucleate acicular ferrite. Galaxite is an oxide that forms on the surface of inclusions and gives a faceted appearance when viewed through the TEM and for which there is minimal disregistry in the Bain orientation. TiN, which also exhibits good registry, has been shown to be effective to some degree as a nucleant of acicular ferrite by Grong et al. [Ref. 6].

Molten phases around the inclusions may be present after the austenite has solidified [Ref. 31]. This molten phase may then oxidize the local austenite matrix. It may also present large thermal induced stresses as this molten phase solidified in a fixed volume between the inclusion and the matrix.

In weld metal compositions where aluminum levels are lower, titanium oxides have been linked to the nucleation of acicular ferrite. The exact oxidation state of these compounds is still in question. Several titanium oxidation states have been noted to cause acicular ferrite in previous research. But to identify one particular titanium component within an inclusion tends to be very difficult due to the thickness of inclusions with respect to electrons so that electron diffraction is difficult and TEM/EDX analysis is a problem because of its inability to determine oxygen with high accuracy.

TiO was reported by Evans [Ref. 21], Babu [Ref. 22] and Abson [Ref. 16] in C-Mn steels. TiO_2 was assumed by Lau [Ref. 17, 19] when investigating HSLA steels. While Ti_2O_3 was found by Kluken and Grong [Ref. 20] who analyzed low alloy steels. Fox and Brothers [Ref. 1] detected a more complex manganese titanate, pyrophanite ($MnO.TiO_2$), along with $MnOAl_2O_3$ galaxite in HY-100 steels. From the above findings it can be seen that the complex inclusion behavior resulting in the nucleation of acicular ferrite is far from being satisfactorily understood. Perhaps Ti exists in several oxidation states, each with an ability to stimulate acicular ferrite to some degree, [Ref. 31].

The character of the inclusions changes as the chemistry of the weld metal is altered. Weld metals containing concentrations of Al tend to have Al_2O_3 or $MnO.Al_2O_3$ galaxite as a core material. When Al is not present in the weld metal, then Mn and Si oxides tend to form instead. Two notable Mn-containing oxides are MnO Manganosite and $MnO.SiO_2$ Rhodonite. Rhodonite is known as a major component of inclusions in steels and steel weld metals with low Al concentrations (<0.005wt%)[Ref. 32].

The sequential oxidation effect proposed by Barley and Pargeter [Ref. 15] and adopted by Bhadeshia and Svensson [Ref. 15] states that reactants will form in the following order within the molten weld pool, Al_2O_3, Ti_2O_3, SiO_2, MnO, TiN and MnS. This sequential formation is consistent with the observation that, in Al-free welds, SiO_2 appears to make up the core of the inclusion. These inclusions tend to exhibit a layered morphology. Where SiO_2 or $MnO.SiO_2$ tend to make up the core of the inclusion an other lower melting temperature compounds such as Ti oxides are deposited on the outer surface.

The overall inclusion size is controlled by oxygen along with the chemical composition of the filler metal. In general, as long as there are deoxidants present, the higher the level of oxygen, the larger the inclusions become. This is due to metallic oxides making up the majority of inclusion components.

Babu et al. 1995 [Ref. 22] proposed that the growth of inclusions in the melt is controlled by the rate of diffusion of oxygen and deoxidization elements toward an oxide nuclei. Babu also notes Ostwald ripening as a contending mechanism in the growth of inclusions within steels. Ostwald ripening was proposed by Kluken and Grong [Ref. 20] as having an effect on the growth of inclusions-once the oxidation process terminates and temperature is falling. At the liquidus line 1811 K the large inclusions grow at the expense of the others.

F. PREVIOUS WORK ON THE CHEMICAL AND CRYSTALLOGRAPHIC ANALYSIS OF THE INCLUSIONS RESPONSIBLE FOR ACICULAR FERRITE

Several researchers have attempted to perform TEM/SEM with EDX analysis on inclusions with some success. The overall composition of inclusions is easily obtainable by EDX. Although accurate light element analysis, in particular oxygen, is difficult. However, this leaves out crystallographic information and specific information on each microconstituent. The probe size required to achieve adequate counts in most EDX equipment is so large that it becomes impossible to distinguish chemical composition of one phase from another. The layered morphology also makes EDX work very difficult

since characterizing x-rays that reach the detector will be from multiple layers of the inclusion.

Electron diffraction has also proved difficult since the steel inclusions are often too thick. In addition, they seem to be too small to etch out to form a colloidal which can be placed in a x-ray diffractometer. The only solution appears to be painstakingly careful work with the thinnest inclusions available using a modern analytical TEM capable of generating very small probe sizes (of the order of 5nm or less) and equipped with both EDX and an electron energy loss spectrometers (PEELS).

Dowling et al. [Ref. 13] had some success in the characterization of nonmetallic inclusions in HSLA steel weld metal using a scanning transmission electron microscope (STEM) with a probe size in the region of 1 to 9 nm. X-ray powder diffraction experiments were also performed but Dowling et al. were unable to match their results to any known standard diffraction patterns. Dowling also performed convergent beam electron diffraction to try to prove epitaxial growth of ferrite on inclusions. No conclusive evidence was formed concerning epitaxial growth despite numerous examinations. The chemical analysis of the inclusions revealed galaxite ($MnO.Al_2O_3$) plus a titanium-rich phase that could have been TiO, TiN or TiC (since they all have the same FCC crystal structure with similar lattice parameters). Dowling et al. suggested that this titanium-rich phase was most probably TiO.

Copper and Sulfur were also detected in Dowling et al.'s inclusions using x-ray microanalysis in the STEM using extraction replicas placed on nickel grids. The exact

ratio of copper to sulfur was not determined in this experiment, but CuS oxide complexes are common in low Al steel weld metal.

Fox, Eakes and Franke [Ref. 31] found that HY-100 steel weld metal inclusions contained MnO, Al_2O_3, SiO_2 and a titanium-rich oxide. These findings were possible by use of a small TEM probe using EDX spectroscopy. From their electron diffraction data Fox et al. went on to suggest that galaxite, $MnO.Al_2O_3$, and pyrophanite, $MnO.TiO_2$, were the major components of the inclusions in the HY-100 steels they studied; these were sometimes complexed with small amounts of MnS.

Babu et al. [Ref. 22] took a thermodynamic approach to the problem. By examining the free energy of each product Babu et al. were able to formulate an empirical equation that provides a time temperature transformation (TTT) curve to predict the formation of microconstituents within weld metal inclusions see Figure (3) and equations (4) and (5).

$$\zeta = 1 - \exp[-(c_m^{\,i} - c_m^{\,i1})/(c_m^{\,1} - c^{i1})\, Iv(\pi/15)(\alpha_3^{*})^3 t^{5/2}] \qquad (4)$$

where

ζ = Extent of reaction

$c_m^{\,i}$ = concentration of the deoxidant within inclusion

$c_m^{\,1}$ = concentration of the deoxidant within molten steel

$c_m^{\,i1}$ = concentration of the deoxidant at the inclusion-steel interface

Iv = nucleation rate-assumed to be homogeneous nucleation

$alpha_3^*$ = parabolic thickening rate constant

t = time

$$\alpha_3^* = [2D_0(c_0^1 - c^{i1})/c_0^i - c^{i1})]^{1/2} \quad (5)$$

where

D_0 = diffusion constant of oxygen in molten metal

c_0^i = concentration of oxygen within inclusion

c_0^1 = concentration of oxygen within molten steel

c_0^{i1} = concentration of oxygen at the inclusion-steel interface

The previous extent of reaction theory is an important milestone in inclusion study. The concentrations of various microconstituents within weld metal inclusions are finally within our ability to predict with some degree of certainty.

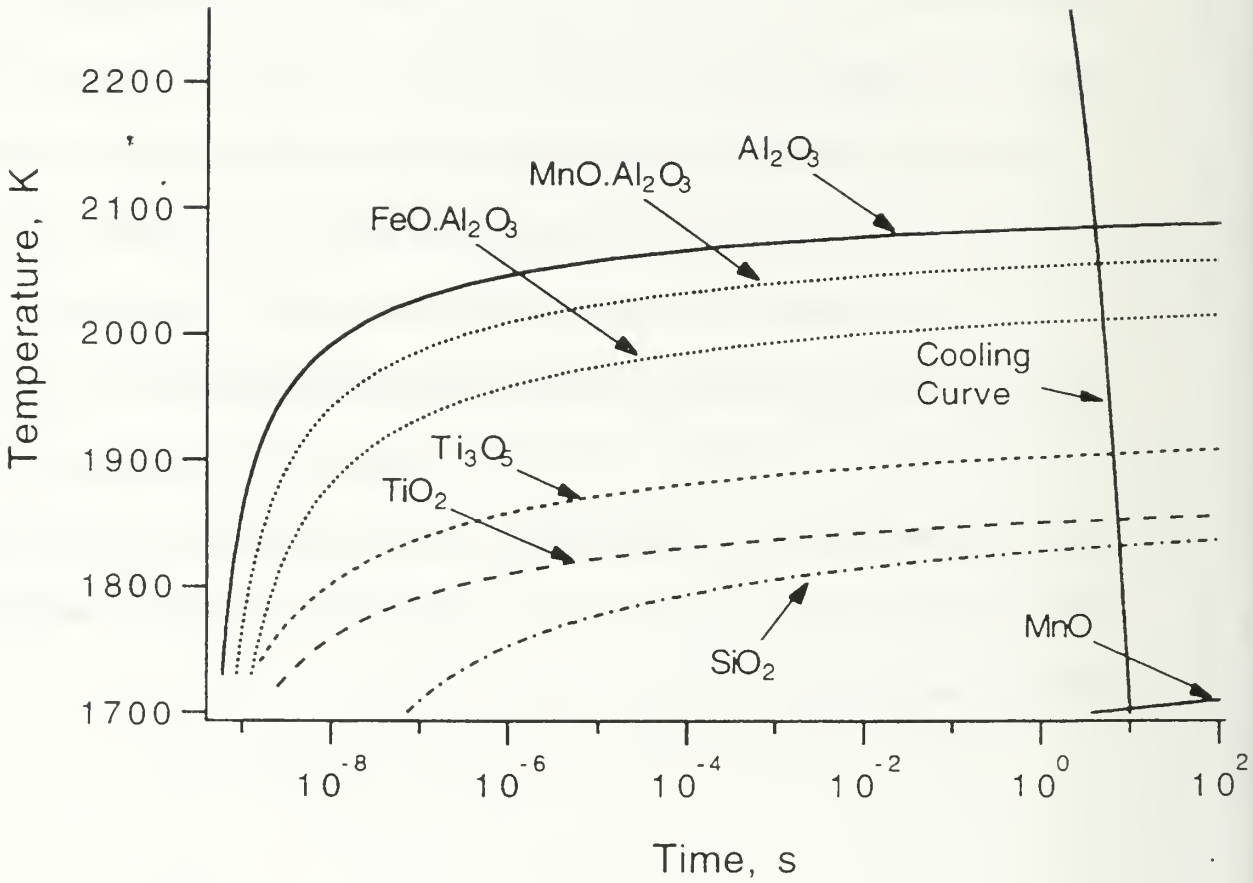

Figure 3 - Time temperature transformation curves generated using Babu et al.'s [Ref. 22] extent of reaction equations.

G. SCOPE OF PRESENT WORK

It is clear from this literature survey that the exact nature of the inclusions responsible for the nucleation of acicular ferrite is not understood. In the present work an attempt will be made to understand the inclusions responsible for acicular ferrite in SMA weldments on C-Mn steel which contains minimal amounts of Al and B so that the predominant deoxidants are Mn and Si. Based on these ideas two welding flux compositions have been used to generate a weld metal chemistry for one weld metal with < 5 ppm Ti and 28 ppm Ti in the other. All other known factors affecting the nucleation of acicular ferrite have been held constant between the two samples. The inclusion size and distribution have been verified to be the same [Ref. 33]. This approach simplifies the chemical compositional variations between the weldment series and will allow a more definitive understanding of how titanium changes the inclusions to nucleate acicular ferrite.

A careful examination of final weld pass non metallic inclusion chemistry on both samples should provide some greatly needed insight into the mystery of titanium-rich inclusions. This investigation will use a Topcon 002B TEM equipped with EDAX EDX spectrometer and Gatan PEELS imaging filter. To determine the size, number and volume fraction of the inclusions scanning electron microscopy will be performed.

III. EXPERIMENTAL

A. PREPARATION TECHNIQUES FOR WELDING AND SUBSEQUENT ANALYSIS

All the SMAW samples were prepared by Dr. G. M. Evans at Oerlikon Welding Limited, Zurich, Switzerland. Detailed sample preparation is given in [Ref. 4] and will be partially reproduced here. All material in this section is contained in [Ref. 4].

1. Electrodes

Titanium metal powder was added to the coatings of basic low hydrogen electrodes to obtain two nominal weld metal titanium levels < 5 ppm Ti (sample O) and 35 ppm Ti (sample W). These two fluxes were then extruded onto 4 mm core wire, the coating diameter to electrode diameter (D/d) of 1.68."

2. Weld Preparation

The joint geometry is specified in ISO 2560-1973. Welding was performed in the flat position with approximately three beads per layer. 27 runs were required to fill the individual joints. Welding parameters were as follows: amperage 170 A in direct current mode (electrode positive), voltage 21 volts and the heat-input was nominally 1 kJ/mm. A standardized interpass temperature was maintained at 200 °C.

3. Heat-Treatment for Testing

Weldments were tested in the "as-welded" condition, All tensile specimens were given a 14 hour 250 °C hydrogen removal heat treatment. Stress relieved toughness specimens were given a 2 hour 580 °C heat treatment.

4. Mechanical Testing

Weldments were cut to provide two all-weld metal tensile specimens (Minitrac) from each of the different deposits. About 35 Charpy-V notch specimens were tested to provide a full reference transition temperature curve

5. Metallography

Weldments were sectioned into transverse slices. All optical examinations were performed on the top beads and on the adjacent reheated zones.

B. SUMMARY OF THE RESULTS PROVIDED BY OERLIKON WELDING LIMITED

Weld metal Chemistry and mechanical property results were also provided by Dr. Evans, Tables (3 and 4). These results were also published in a paper by Cerjak et al. [Ref. 33]. The chemistry results in Table (3) are of the last pass of the weld metal in the "as-welded" condition.

Table 3 - Chemical Composition of Samples "O" and "W"

	C	Mn	Si	S	P	Ti	B	Al	N	O
	%					ppm				
O	0.074	1.40	0.25	0.008	0.007	1	1	6	79	475
W	0.077	1.46	0.27	0.008	0.007	28	3	5	81	459

All chemical analyses were performed in the area of the last weld bead. This prevented variations due to dilution effects, which are common in multipass welds with chemical differences between the filler wire and the base plate.

Mechanical properties listed in Table (4) contain both "as-welded" and post weld heat treatment (PWHT) properties which are specified in part A.3 above.

Table 4 - Mechanical Properties of Samples "O" and "W"

	As-Welded					After PWHT		
	YS	UTS	EL.	RA	ISO-V,	Celsius	ISO-V,	Celsius
	MPa	MPa	%	%	100 J	28 J	100 J	28 J
O	445	528	28.2	78.0	-14	-42	-74	-97
W	471	544	25.2	77.0	-68	-88	-70	-90

C. MECHANICAL FINISHING OF SAMPLES

One inch thick transverse slices were cut from both weldments. Surface polishing was performed by progressively machine grounding, using 180, 320, 500 and 1000 grit silicon carbide paper. The slices were further polished using diamond oxide paste at 3 micron, followed by 0.5 micron silicon oxide compound.

D. OPTICAL MICROSCOPY

1. Analysis Objective

Optical microscopy provided insight into the nature of the acicular ferrite morphology and allowed a check on the work of Cerjak et al. [Ref. 33].

2. Optical Etchant

Samples were etched for 10 seconds using 5% nital (5% nitric acid and 95% methanol). This etch reveals the various microconstituents including acicular ferrite and Bainite. Micrographs are shown for each microstructure (Figures 4 through 7). All photographs were taken on a Zeiss Jenaphot 2000 Optical Photomicroscope using 35 mm film and a digital capture camera.

Graphs of acicular ferrite (A.F.), sideplate ferrite (S.P.F. or Bainite) percentages were also provided by Evans and are reproduced below Figure (8). Cerjak et al. [Ref. 33] calculated A.F. microstructural percentages by manual point count in accordance with [Ref. 7].

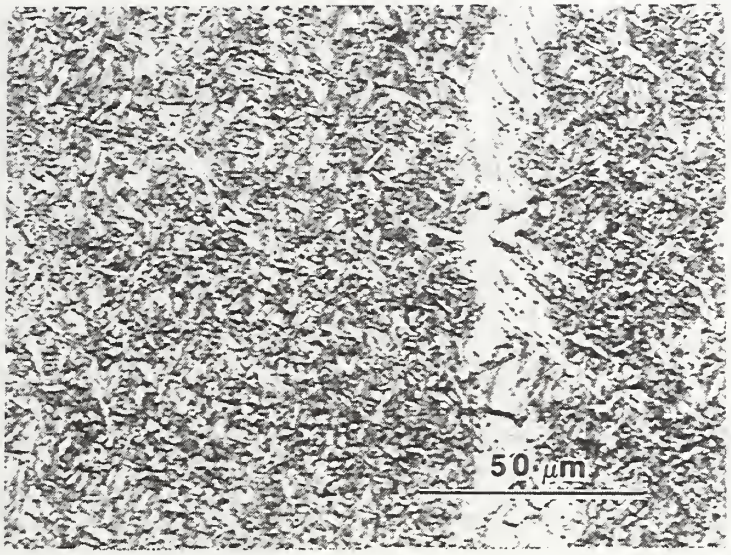

Figure 4 - Optical micrographs taken from the final weld pass of sample W (Ti-rich).

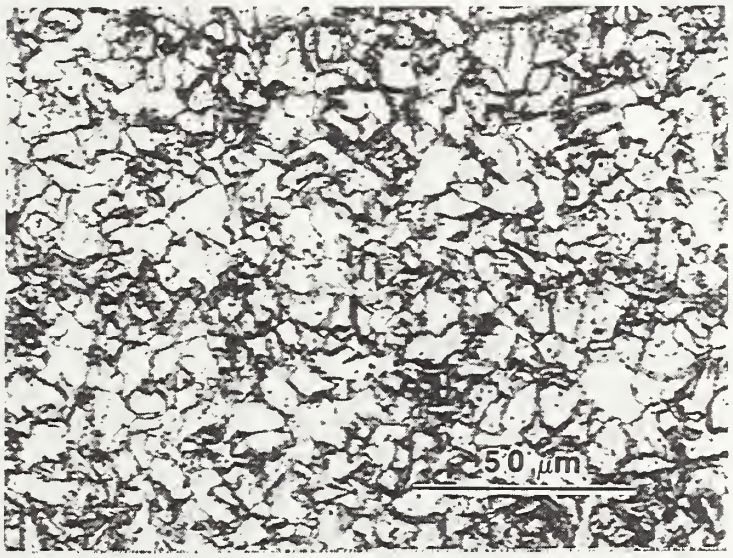

Figure 5 - Optical micrographs taken near the first weld pass of sample W (Ti-rich).

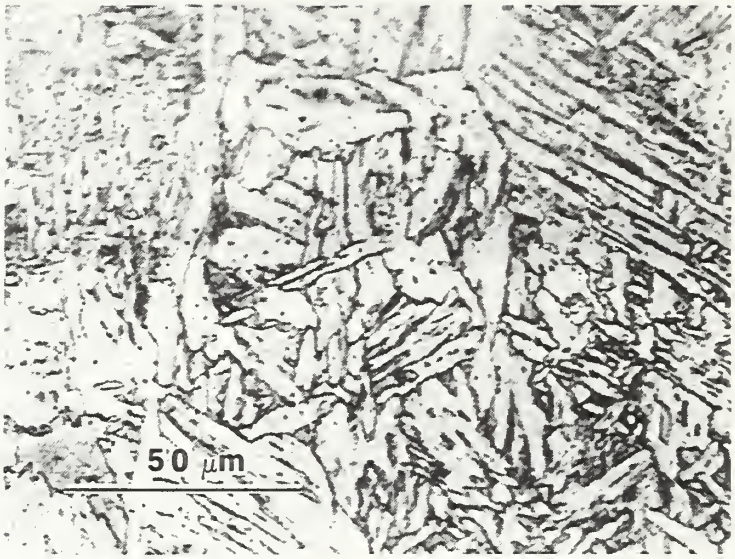

Figure 6 - Optical micrographs taken from the final weld pass of sample O (Ti-free).

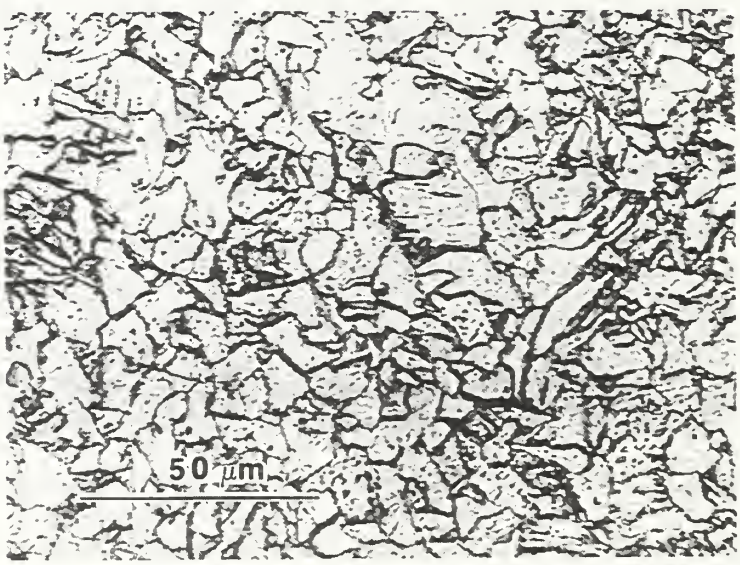

Figure 7 - Optical micrographs taken near the first weld pass of sample O (Ti-free).

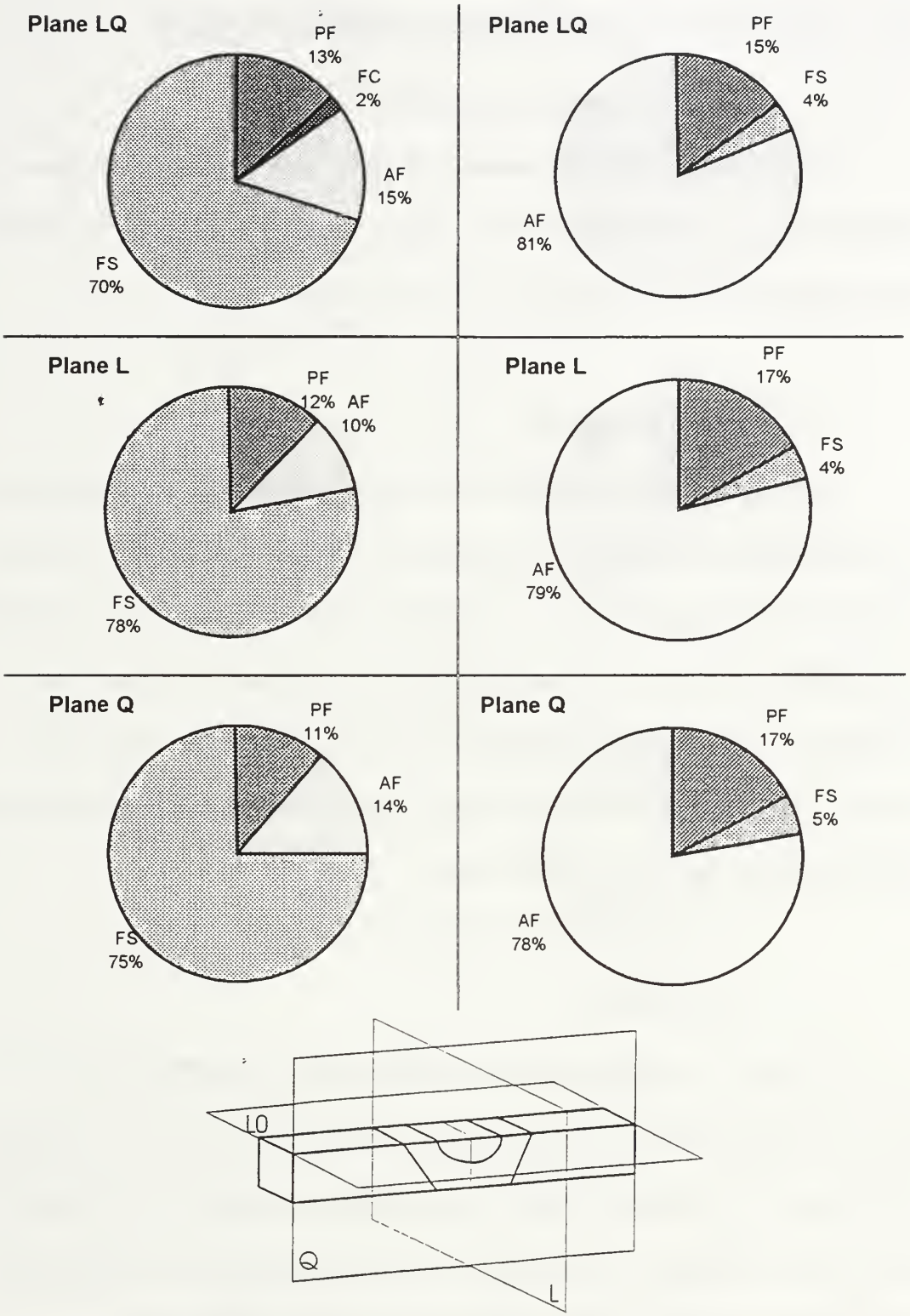

Figure 8 - Multi-plane microstructural analysis performed by Cerjak [Ref. 33].

E. SCANNING ELECTRON MICROSCOPY (SEM)

1. Objective of SEM Investigation

SEM analysis provides information on inclusion size, distribution and shape. This was performed as a verification to ensure inclusion volume fraction, size and distribution were essentially the same between the two weldment series.

2. Sample Preparation

Transverse weldment samples were placed in the Cambridge Stereoscan S200 scanning electron microscope with unetched faces. Samples were stored in a vacuum container with desiccant to reduce corrosion which has been noted by previous researchers as a possible source of inclusion measurement error. Microscope parameters were 20 kV accelerating voltage for a magnification of 5820X with a working distance of 9 mm. The microscope was operated in backscattered electron mode to obtain high resolution atomic number contrast when working with inclusions.

3. SEM Overview

In the scanning electron microscope (SEM), electrons are emitted from a source, such as a Lanthanum hexaboride crystal and accelerated to about 200 kV. The electrons are focused on the sample by magnetic lenses which are controlled by a scanning device that moves the beam in successive passes across the sample Figure (9). This pattern is much the same as a video monitor updates its screen and is called a raster.

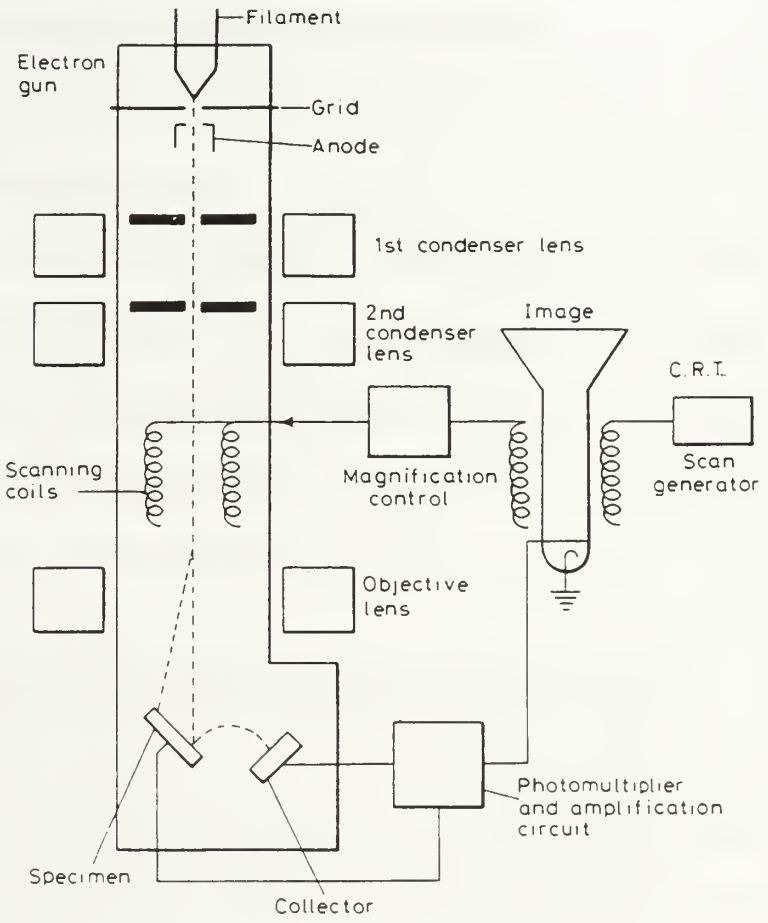

Figure 9 - Physical arrangement of an SEM

The electrons strike the surface of the sample and interact with the material, see Figure (10). These interactions lead to the emission of secondary electrons, backscattered electrons and x-rays that are used to generate images or identify chemical elements. Secondary electrons leave the surface of the sample with an energy of 50 eV or less. They are created by charged particle interactions between incident or primary electrons with the

sample or they can be primary electrons that inelastically scatter back toward the sample surface.

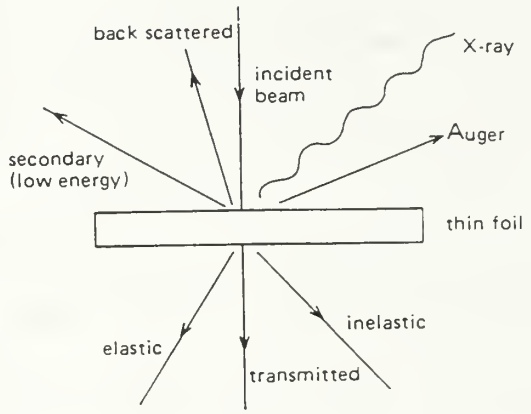

Figure 10 - Electron sample interactions.

Backscattered electron are incident electrons that leave the sample surface with large fractions of their initial energies after essentially elastic interactions the backscattered intensity is generally lower than secondary electron intensity.

Both characteristic x-rays and Bremsstrahlungen (background) are emitted from the excited atoms. Bremsstrahlung is a German term for braking radiation and it is caused by the deceleration of charged particles through a electric field such as the field surrounding an atom. The characteristic x-rays which are used for chemical microanalysis arise as a result of atoms which have experienced an ionizing event leaving an inner shell vacant and an outer shell electron drops into the orbital releasing energy in the form of a characteristic x-ray. The intensity of these characteristic x-rays may then be measured

which together with the intensities of all other characteristic x-ray emissions they can be used to calculate the chemical compositions within an unknown sample.

4. Inclusions in Steels

In order to count and size inclusions it is useful to image them in backscattered electron mode. The backscattered electron detector is sensitive to the electrons that are scattered back toward the electron emission source and high intensity scattering shows areas of high atomic number and/or high sample density as lighter contrast. Inclusions show up dark with a light background in this mode. See Figure (11).

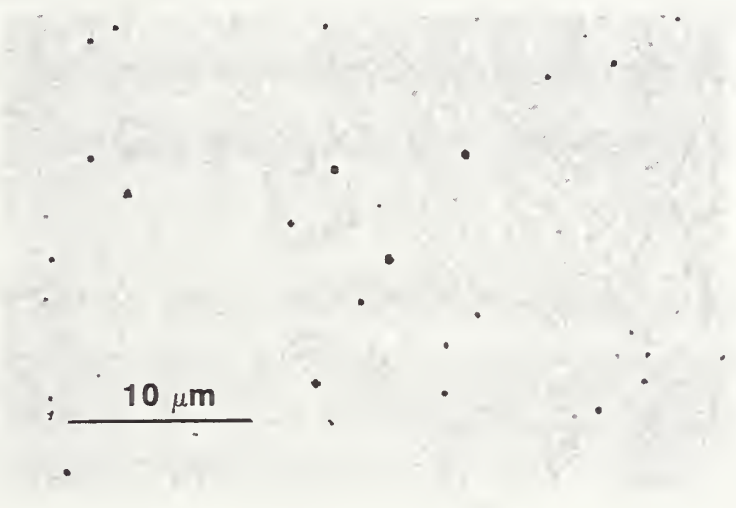

Figure 11 - Backscatter SEM micrograph of an inclusion.

5. Analysis

The inclusions were counted and measured using the SEM on screen cursors. This allows inclusion sizing within the limits of the microscope resolution (about 100 nm in

backscatter mode). One hundred fields were counted. A mean value of number of inclusions per field and diameter was calculated along with a 99% confidence value for the diameter measurement's statistical error. By determination of the area of the field of vision and with a knowledge of the mean inclusion diameter and number, the volume fraction of inclusions in the weldment can be calculated. This volume fraction was calculated in accordance with Quantitative Microscopy [Ref. 7]. An assumption was made that any transverse slice of the sample would contain the same concentration of inclusions near the weld centerline.

Of the one hundred fields analyzed, all inclusions greater than 0.150 micron in diameter were recorded. The average diameter, number of inclusions per field volume percent and standard deviation are listed in Table (5) and it is clear that the size distribution and volume fraction are almost identical for both samples.

Table 5 - Inclusion Distribution within Samples "O" and "W"

	Average size in microns	average # inclusion/field	confidence	standard deviation	volume fraction
Sample "O"	0.30555	10.70	.00993	.12619	0.00223
Sample "W"	0.30554	10.90	.00799	.10247	0.00227

The volume fraction was calculated using the equation: [Ref. 7]

$$\text{Volume Fraction} = (s \pi d^2)/(4 f) \qquad (6)$$

where

s = average number of inclusions per field

f = inclusion field size

d = mean diameter of inclusions

The field of view was calculated from the magnification and the display area of the (SEM), at 5800X it is 3.521 x $10^{-10}/m^2$. The volume fraction calculation assumes an equal probability that a polished plane contains the same volume percentage as any other plane in sample [Ref. 7].

Any statistical analysis that incorporated a confidence calculation was performed by:

$$\text{Confidence} = +/- 2.57\ (\sigma\ /\text{SQRT}(n)) \qquad (7)$$

where

n = population

$$\sigma = \text{standard deviation} = [(n\Sigma x^2-(\Sigma x)^2)/n(n-1)]^{1/2} \qquad (8)$$

Where x is the range on either side of the sample mean that 99% of all data should exist.

F. TRANSMISSION ELECTRON MICROSCOPY (TEM)

1. Objective of TEM Analysis

One of the most effective tools available to investigate the morphology, crystal structure and chemistry of welding inclusions is the TEM used in conjunction with energy dispersive x-ray spectroscopy (EDX) and parallel electron energy loss spectroscopy (PEELS). Each of these chemical analysis methods has advantages over the other. It is beneficial to use one characterizing method to complement the other in order to improve the likelihood of a correct chemical analysis.

Both carbon extraction replicas and standard electropolished samples were prepared for analysis in the TEM. Carbon extraction replicas tend to provide thinner inclusion areas with no magnetic interference from the surrounding matrix to distort the electron beam used in the TEM. Thin samples are of fundamental importance since sample thickness can lead to excess absorption of emitted x-rays and consequent difficulties with light element analysis. Thin samples are also necessary for PEELS analysis.

Standard electropolished samples could possibly provide information on the orientation and chemical relationships between the inclusion its associated steel matrix and so these were also prepared. The inclusion chemistry obtained from EDX performed on the inclusions in carbon extraction replicas were compared with EDX on the inclusions in electropolished samples to ensure the inclusions were not being altered by the extraction process.

PEELS can provide five types of information.

- Qualitative chemical composition
- Quantitative chemical composition
- Sample thickness
- Energy loss near edge fine structure (ELNES)

ELNES provides information on the nature of electronic bonding within the sample. i.e. near-neighbor coordination information.

- Extended energy loss fine structure (EXELFS)

EXELFS occurs in the higher energy loss region of an ionization edge. The extended energy loss edges oscillate due to short range order effects within the crystal lattice caused by ejected electrons scattering with nearest neighbor atoms.

A thorough investigation of the inclusion chemistry using EDX and PEELS may thus give insight into the complex mechanisms that that lead to the formation of the microconstituents within the layered morphology of the nonmetallic inclusions.

2. Preparation of Carbon Extraction Replicas

Carbon extraction replicas were produced by etching the transverse weld face of each sample for 25 seconds in a solution of 5% nital. This removes some of the steel matrix exposing the hard non-reactive ceramic inclusions. The etched samples were then cleaned with ethanol and masked such that only areas of interest, i.e. the last weld pass, were revealed. The samples were then placed in a Ernest F. Fullan Mk II carbon coater. Two carbon strands were placed 300 millimeters above the etched faces of the sample. Once the chamber was evacuated a current was passed through the carbon strands depositing a fine layer of carbon on the weldment. Two millimeter squares were scribed into the carbon layer using an awl. The masking material was then removed, and the samples were placed in a bath of 5% nital for extended etching. Within five minutes the squares began to float off. Since the steel matrix was etched away below the inclusions. The inclusion-carbon sheets were left loose in the acid solution. Carbon-inclusion squares were then collected and placed in a solution of methanol. The methanol cleaned the

carbon sheets of acid and tended to flatten out the squares. The flattening effect is due to the surface tension, making them more easily gathered for placement on nickel grids. Nickel grids were selected rather than copper because previous research [Ref. 31] had revealed copper in similar inclusions in steel weld metal.

3. Electropolishing of Samples for TEM

The one inch sections of the weldment were sliced again transversely into 1 millimeter slices using a high speed diamond saw. This cutting process was monitored carefully to minimize frictional heat buildup in the sample. Heat buildup, may alter the condition of the "as-welded" microstructure, interfering with any later microstructural or chemical observations.

These thin slices were then mounted on phenolic pucks and ground by methods similar to those stated in the mechanical finishing section. Surface polishing was terminated once the slice thickness reached about 100 microns. The slices were then removed from the pucks by soaking in acetone solution. A thorough wash with methanol was performed to remove any residual acetone. Three millimeter round disks were then punched out of the slice in the area of the last weld pass. These three millimeter disks were then further thinned by use of the Gatan 623 disk polishing unit. One thousand grit silicon carbide sanding medium was used in the thinning process. Once a uniform thickness of 40 to 50 microns was achieved samples were cleaned in methanol in preparation for electropolishing.

Electropolishing was performed using an E. A. Fischione instrument manufacturing company, twin jet electropolisher. This polisher was operated at a potential of 75 volts in a solution of 3% perchloric acid, 35% butanol and 62% ethanol at minus 20 °C. The sample current during electro polishing was noted to be 50 milliamps. Polishing was performed until a small hole developed toward the center of the sample as indicated by a photodetector. The detector sensitivity was first adjusted by the use of a standard with a known hole size. After a preliminary setting was made to the apparatus, several runs were performed and subsequent adjustments made to obtain desired hole size and edge thickness. The final examination of the polished samples revealed a tiny hole near the center of each sample. The material near this hole was on the order of 50-100 nm thick. This is acceptable for most TEM analysis.

4. Brief Description of a TEM

TEMs are capable of imaging and chemical microanalysis with high spatial resolution. High resolution images are formed because accelerated electrons have a short wavelength (2.73 pm at 200 kV) and with the Topcon 002B used in the present work the limit of spatial resolution in images is about 0.18 nm. For microanalysis the smallest electron probe (spot) diameter useable is around 5 nm for EDX analysis and about 1 nm for PEELS. This makes the TEM a very powerful tool for the analysis of materials since virtually simultaneous imaging, diffraction and chemical microanalysis at high resolution can be performed.

The general layout of a TEM column is provided in Figure (12). This column is evacuated to around 10^{-7} Torr so that the electrons are not scattered by air molecules. The electrons are emitted from an electron gun then focused on the sample by the condenser lenses. The image of the sample is magnified by an objective lens and several projector lenses (usually three or four) so that the final image is observed on a phosphorescent screen near the bottom of the column. The transmitted electrons strike the phosphorescent screen and a transmission image of the sample is formed.

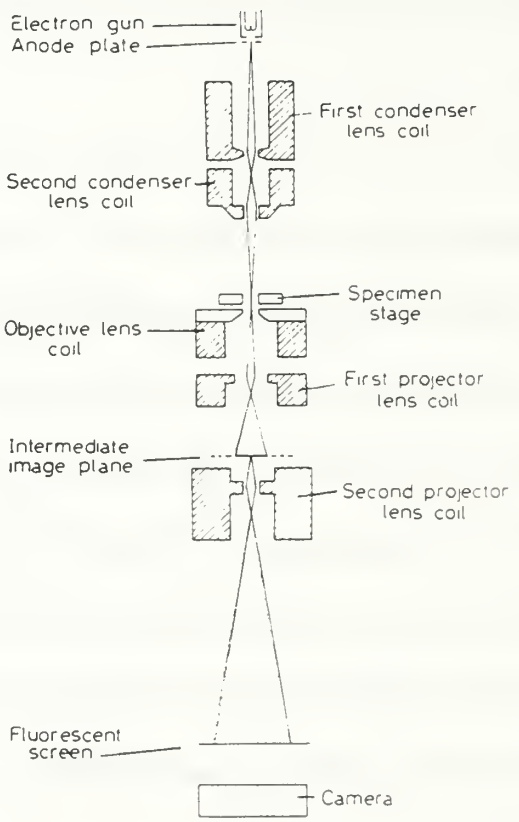

Figure 12 - Schematic of TEM optics.

Imaging and diffraction are accomplished with different lens configurations. Figure (13) shows the two basic lens configurations for each of these modes of operation. By manipulation of the objective and projector lens currents, the electron ray paths can be adjusted to produce an image or an electron diffraction pattern on the fluorescent screen.

Objective apertures may also be used to produce dark or bright field images Figure (14). One of these apertures can be placed in the back focal plane of the objective so that either the direct or the transmitted beam.

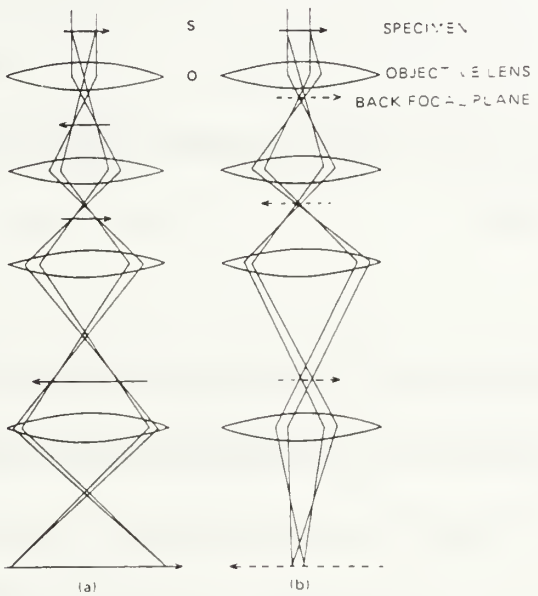

Figure 13 - TEM magnetic lens arrangement for diffraction (a) and imaging (b).

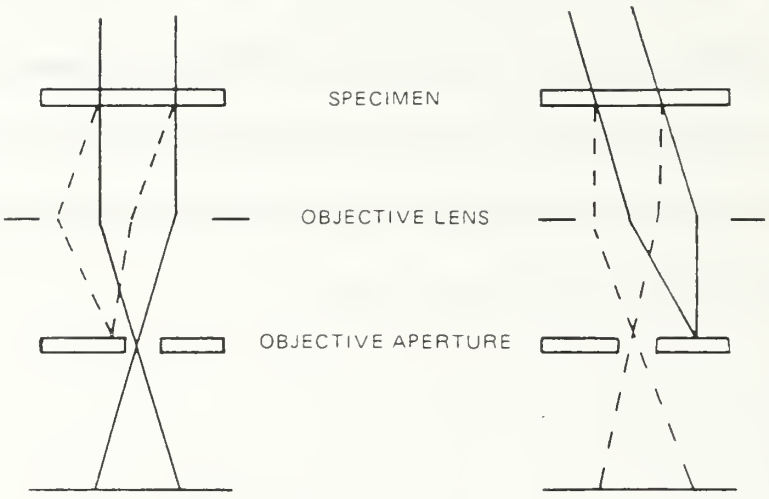

Figure 14 - TEM apertures insertion operation for bright (left) and dark (right) field imaging.

contributes to the final image. During bright field imaging the diffracted electrons are excluded and only the direct beam contributes to the final image. Dark areas in the image thus show areas of high diffraction or absorption. In dark field imaging the aperture is again placed at the back focal plane, but it is used to block the direct beam and it allows the information from one diffracted beam to pass. Here, the areas in the image that are diffracting show bright and regions that are not, show dark. Imaging using diffraction contrast can provide great insight into the nature of defects such as dislocations, grain boundaries and precipitates.

Conventional "spot" electron diffraction patterns arise from the Bragg diffraction of the electron waves (elastic scattering). Since this occurs at small angles (1 or 2 degrees) with very short wavelength electrons, the pattern from a single crystal region of a sample is from sets of planes which belong to the same crystallographic zone.

A typical spot pattern is shown in Figure (15). The electron interactions that are responsible for this phenomenon are governed by Bragg's law:

$$\lambda = 2d\sin\theta \qquad (9)$$

where

λ = wavelength of electrons

d = distance between planes of atoms

θ = angle of diffraction

a simplification of this law for small θ is

$$d_{HKL} = \lambda L/R_{HKL} \qquad (10)$$

where

d_{HKL} is the distance between atom planes with Miller indices (hkl)

R_{HKL} is the distance from the undiffracted to diffracted spots (hkl)

L = camera length

λ = electron wavelength

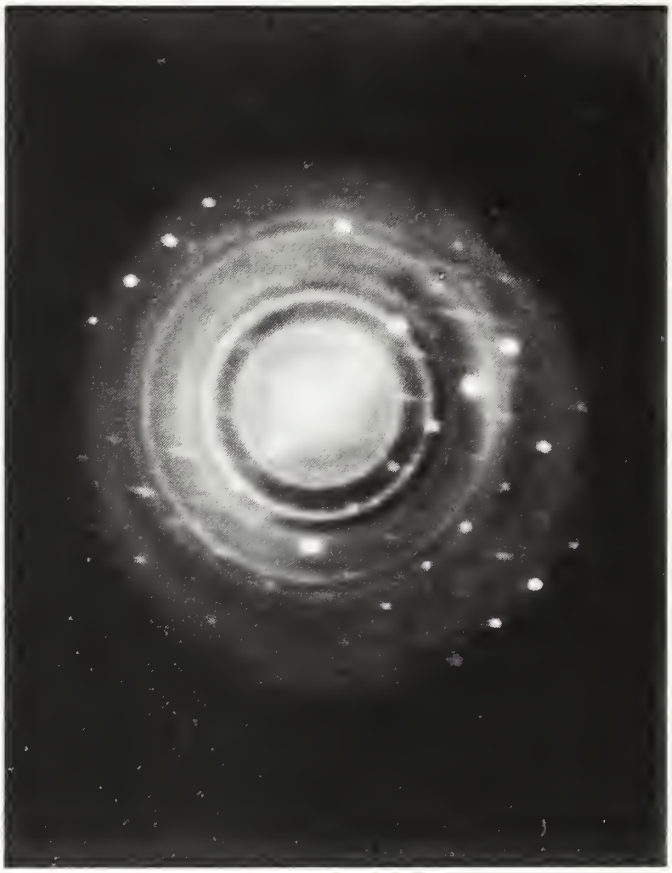

Figure 15 - Typical electron spot diffraction pattern for a Ti-free inclusion in C-Mn steel weld metal of the present work.

5. Electron Beam Interactions

As electrons strike the sample there are several interactions that they may undergo. The use of elastically scattered electrons to produce diffraction patterns and images under conditions of diffraction contrast was described above. The interactions of interest are shown in Figure (10). Electrons which strike the sample may be scattered in seven different ways.

Incident electrons may interact with sample atoms to ionize an inner shell electron. An outer shell electron may then reduce its energy and fill this inner shell vacancy. The atom then has an excess of energy, which it can emit one of two ways.

- A characteristic x-ray may be emitted.

- An Auger electron may be ejected.

In either case the energy of the x-ray or Auger electron of quantized and related to the difference in energy between an outer and inner electron orbit.

Electrons may also be backscattered. That is, electrons may interact with the sample's atoms and be elastically scattered back at high scattering diffraction angles as in the SEM.

Secondary electrons may also be emitted. These are low energy electrons that may have been generated by several processes. Secondary and backscatter detectors are normally only fitted to SEMs, but in some cases they have been fitted to TEMs.

The final section on electron interactions is concerned with electrons that pass through the sample. Electrons may be elastically scattered (diffracted), inelastically scattered or merely transmitted through the sample without under going any interactions.

6. Exploitation of X-ray and Energy Loss Signals

X-rays may be detected using an energy dispersive x-ray (EDX) detector. These x-rays, as stated before, contain the energy evolved from an outer shell electron giving up energy to fill an inner shell vacancy. This energy can be measured by a lithium drifted silicon, (SiLi), detector. EDX spectroscopy will be discussed later.

Electrons which are inelastically scattered by the sample are detected to provide an indication as to chemical composition. Both qualitative and quantitative results are possible using this method. More on this subject will be provided in the parallel electron energy loss spectrum (PEELS) section.

7. Summary of Energy Dispersive X-ray (EDX) Spectroscopy

The electrons that bombard the sample can cause ionizing events that lead to the emission of both characteristic x-rays and Bremsstrahlungen. The characteristic x-rays arise when outer shell electrons give up energy as they fill inner shell vacancies caused by ionization events. The energy of the x-ray is quantized and thus each element in the Periodic Table has its own characteristic x-ray spectrum.

These x-rays may be collected as shown in Figure (16) then read by a detector as in Figure (17). The SiLi detector usually has a thin window of Be or mylar or similar strong, light material to prevent condensation of hydrocarbons and water vapor on the detector surface. The x-rays pass through this window and produce electron-hole pairs in the SiLi. 3.8 eV of energy is required to form an electron-hole pair. The electrical pulse associated with the electron-hole pairs is amplified and fed to a multi channel analyzer (MCA). The intensity or counts are provided in graphical form plotted against energy Figure (18) shows a typical EDX spectrum. From such a spectrum a qualitative assessment of the elements present in the sample may be immediately made by noting the energies of the characteristic lines.

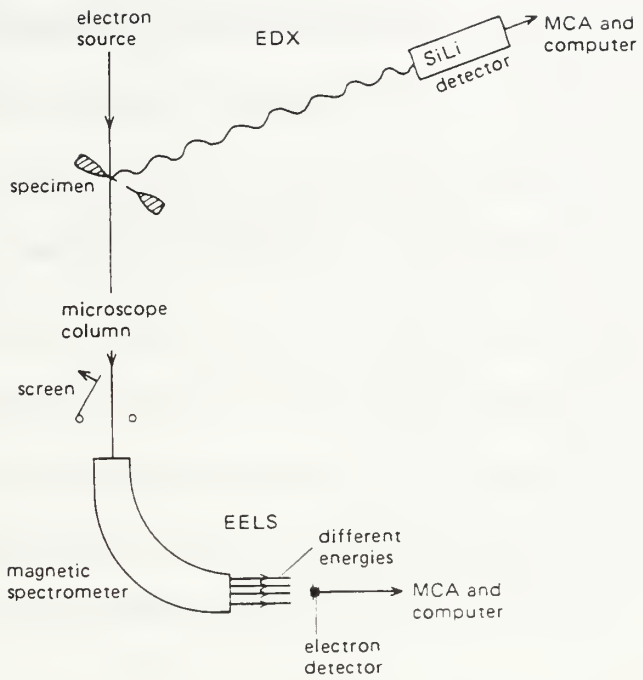

Figure 16 - EDX and PEELS detector arrangement

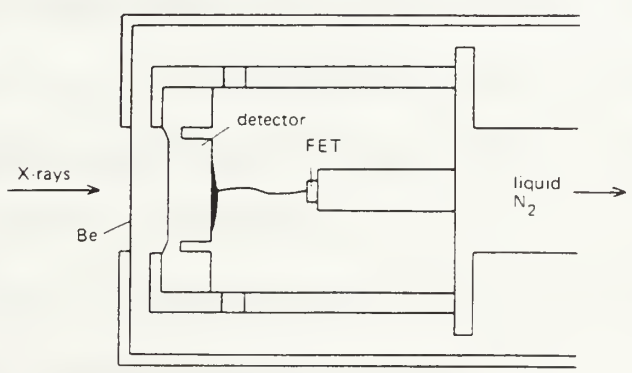

Figure 17 - SiLi EDX detector

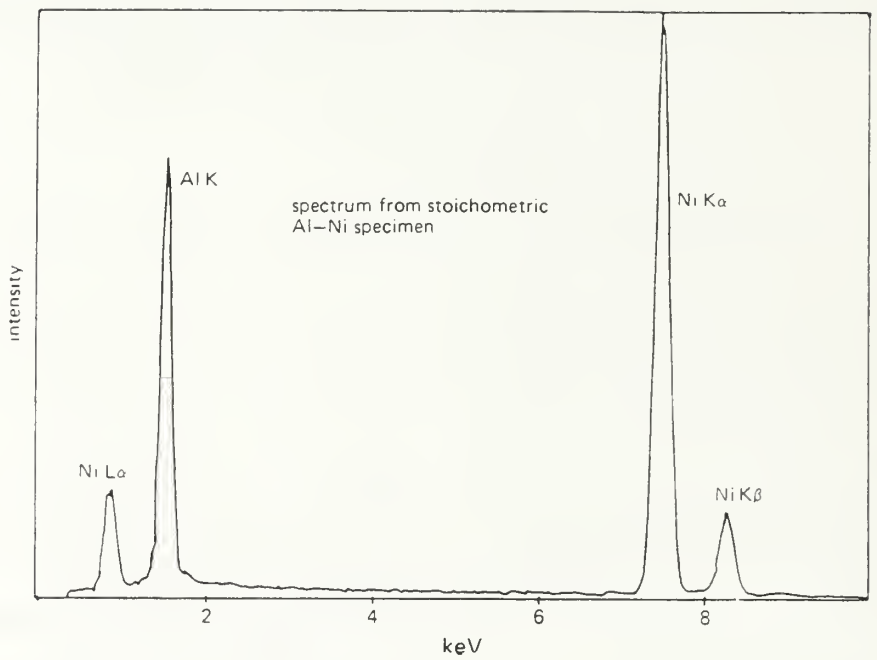

Figure 18 - Typical EDX spectrum

Corrections must be applied to the characteristic intensities in EDX spectra to obtain quantitative results. These corrections are centered around three major issues, atomic number, absorption and fluorescence.

The atomic number, or Z-correction, takes into consideration the differences in x-ray intensity associated with atoms of different atomic number in the sample.

Absorption also plays a role in quantitative EDX. As the sample becomes relatively thick, x-rays must travel a longer path before they emerge from the sample surface. X-rays of different energy will be attenuated differently on this path-thus there

can be a significant correction for lost intensity of lower energy x-rays (light elements) in thicker samples.

If a sample containing elements A and B is subjected to an electron beam and element A emits characteristic x-rays these x-rays may then excite the characteristic x-rays of element B atoms (or vice versa), this phenomenon is called x-ray fluorescence. This, of course means that the x-ray intensity from element B atoms is artificially elevated.

Fluorescence is most pronounced when there is an atomic number plus 2 or (Z + 2) separation between elements A and B. The classic example of fluorescence is the Fe-Cr system where the thicker the sample (more probability of x-ray absorption) the higher the Cr concentration appears [Ref. 23]. For this very reason fluorescence must be accounted for in EDX analysis.

The previous three corrections, atomic number (Z), absorption (A) and fluorescence (F) are together referred to as the (ZAF) correction. EDX work using these corrections without standards can provide an accuracy in chemical analysis within +/- 1% if care is taken.

Quantitative EDX is based on ratios of x-ray intensities. If a sample contains elements A and B then the intensity of the x-rays measured from A to that measured for B will yield the relative percentages of A to B in the sample. In equation form this can be written:

$$n_A/n_B = (I_B Q_B W_B a_B Z_B)/(I_A Q_A W_A a_A Z_A) \qquad (11)$$

where

n = number of atoms

I = intensity of x-rays

Q = Ionization cross section

W = fluorescent yield

a = fraction of K, L or M line that is collected

Z = efficiency of detector

Note that these values may be different for each element as indicated and use of this and is thus really only applicable to very thin samples.

8. Difficulties Associated With Low Atomic Number Elements

Light elements are difficult to quantitatively measure because of poor fluorescent yield, sample absorption of low energy x-rays prior to reaching the detector and poor detector efficiency with low energy x-rays.

Elements that are excited by electron bombardment may emit an x-ray or eject an Auger electron. This emission/ejection process is competitive in nature. Lighter elements tend to eject Auger electrons more often than emit x-rays. Because of this, light elements are said to have poor fluorescent yield. This reduction in characteristic x-ray emission contributes to poor signal to noise in EDX analysis of lighter elements.

Lower energy x-rays are thus more likely to be absorbed in the sample as it travels toward the surface. This means that relatively fewer light element x-rays leave the surface of the sample.

Finally the light element x-rays that do reach the detector are of such low energy that they may be attenuated by the detector window or if they actually make it to the detector because of their lower energy they create fewer electron hole pairs. This also translates into a lower signal to noise ratio. Equation (11) does not take into account absorption and fluorescence.

To attempt to overcome light element detection problems standards may be employed. The use of a standard allows the detector to be calibrated for light elements. A calibrated EDX detector may then be used for the analysis of samples with a similar chemical composition and thickness. It is obviously necessary to choose a sample for which the ZAF corrections will be similar. For oxide analysis this method can work exceptionally well.

In the present work the typical steel weldment inclusions contain $MnO.SiO_2$ Rhodonite. Sample O has been welded with titanium free electrodes. Its inclusion chemistry shows a 1:1 Mn to Si ratio with approximately 60 at% oxygen which is well characterized (see later). Thus, by using sample O as an EDX standard the chemical composition of sample W can be determined.

9. Parallel Electron Energy Loss Spectrum (PEELS)

Figure (19) shows a typical PEEL spectrum. There are several features to note in this Figure. To gain a basic understanding of PEELS a brief overview of each of the major electron interaction responsible for features of the spectrum is necessary.

a. The Zero Loss Peak

The zero loss peak contains the information about electrons which have not lost energy (elastically scattered) or lost very little energy within the limit of resolution of the PEELS detector. Electron-phonon interactions are therefore also included in the zero loss peak.

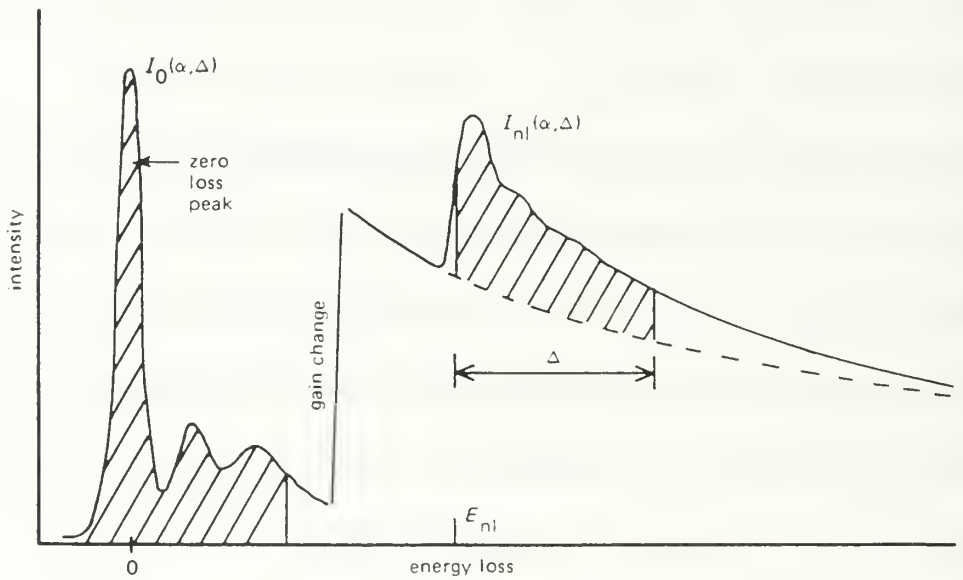

Figure 19 - Typical PEELS spectrum

b. Plasmon Loss Peaks

The plasmon loss region starts at 2 eV and extends up to about 50 eV. Plasmons are longitudinal wave-like oscillations of the weakly bound electrons in the sample. As the electron beam travels through the sample it will excite weakly bound valence electrons as plasmons and experience losses. The mean free path associated with plasmon losses is about 50 nm and thus sample thickness data can be obtained from this region.

c. Characteristic Ionization Losses

The high loss region can extend up to several keV. It contains the characteristic ionization loss edges along with a continuous background. There are also Compton scattering losses contributing to the background. Qualitative chemical analysis may be performed by measuring the edge losses and comparing them to known standard edges. The fine structure of these characteristic peaks can give information concerning the chemical state of the elements present. Just as the edge energy provides information concerning the elements within the sample, the position of the edges and their fine structures also provides characterizing information. Consequently studies of the energy loss near edge fine structure (ELNES) can identify elements and how they are coordinated in their crystal structure.

The near edge fine structures can change if the excitation energy required to jump from an inner shell to a valence shell changes and/or the number of available valence shells changes. This means that a change in chemical state, e.g. if TiO oxidizes

and goes to TiO_2, the number of valence shells available changes. The change in shape and energy of the Ti and O ionization edges allows the chemical state of the titanium oxide to be discernible by ELNES.

Extended energy loss fine structure (EXELFS) in the higher energy loss region of edges appears as oscillations in the extended edge structure, Figure (19). These oscillations are due to short range order effects within the crystal lattice. This due to electron interactions involving ejected electrons scattering with nearest neighbor atoms. This analysis can be hindered in thick samples by plural scattering. Using EXELFS a calculation of the interatomic distances between the nearest-neighbor atoms is possible.

d. Use of EDX and PEELS in the Present Work

EDX can provide excellent chemical analysis with an electron probe diameter as small as 5 nm in the 002B TEM. This resolution is usually more than adequate for inclusion analysis. The problem with EDX alone is that there is little information about the near-neighbor coordination of the atoms present. All compound identification must be done by intensity ratios and ZAF corrections. In situations where multiple unknown oxides exist, a means of identifying valencies is desired since it is often difficult to measure oxygen accurately by EDX because it is a light element.

The 002B TEM fitted with PEELS can identify oxidation states of many elements [Ref. 34] with a limit of spatial resolution of around 1 nm. This is achieved by using a qualitative analysis of elements present and ELNES to fingerprint the electronic structure of compounds.

In the present work a general chemical analysis of the inclusions will be performed by TEM/EDX and compound fingerprinting by PEELS will be used if the need arises. In particular the oxidation state of the titanium in the inclusions needs to be determined and this will be attempted by both EDX with standards and by examining the ELNES structure of the Ti L and O K edges in the PEEL spectrum.

IV. RESULTS AND DISCUSSION

A. MECHANICAL PROPERTIES

Mechanical properties testing was performed by Cerjak et al. [Ref. 33]. The results are shown in Table (6) below.

Table 6 - Mechanical Properties of Samples "O" and "W" [Ref. 33].

	As-Welded						After Stress Relief heat treatment	
	YS	UTS	EL.	RA	ISO-V,	Celsius	ISO-V,	Celsius
	MPa	MPa	%	%	100 J	28 J	100 J	28 J
O	445	528	28.2	78.0	-14	-42	-74	-97
W	471	544	25.2	77.0	-68	-88	-70	-90

100 J and 28 joule Charpy-V notch temperatures are shown. The data listed relates shelf temperatures to corresponding fracture energies. The data has been separated into two categories; "as-welded", the mechanical properties of the weld bead without any heat treatment and post weld heat treatment (PWHT). The PWHT was 580 °C for 2 hours.

The PWHT was performed to relieve any residual stresses with in the weldments prior to impact testing. This shift in mechanical properties is attributed to the acicular ferrite concentration. Sample W which will be shown later has a significantly higher acicular ferrite content and also has superior "as-welded" toughness therefore does not require a PWHT.

Yield strength data is also shown in Table (6). All samples for tensile testing were subjected to a 2 hour 250 °C hydrogen removal heat treatment. Note the increase in the yield strength of sample W as compared with the titanium-free sample O. This increase in yield strength is linked to the high content of fine acicular ferrite platelets and their associated dislocations.

B. WELD CHEMISTRY RESULTS

As discussed previously, weld metal chemical analysis was supplied by Dr. G. M. Evans, Table (7). Great care has been taken to obtain weldments with extremely low Al content. By reducing Al content to this level (<6 ppm) Al_2O_3 and $MnO.Al_2O_3$ should not form in appreciable amounts, thus only Ti, Mn and Si oxides will be present to nucleate acicular ferrite. This will hopefully reduce the complexity of the inclusion analysis.

Table 7 - Chemical Composition of Samples "O" and "W" [Ref. 33].

	C	Mn	Si	S	P	Ti	B	Al	N	O
	%				ppm					
O	0.074	1.40	0.25	0.008	0.007	1	1	6	79	475
W	0.077	1.46	0.27	0.008	0.007	28	3	5	81	459

C. ACICULAR FERRITE CONTENT

Qualitative optical microscopy was performed on the weld samples to estimate acicular ferrite content. All quantitative measurements of acicular ferrite content were also performed by Cerjak et al. [Ref. 33]. Microstructural identification was performed using [Ref. 35]. The manual point count survey was performed in accordance with [Ref. 7].

Results are as follows; Sample O contained ~ 12 % acicular ferrite while the majority of the structure was ferrite with a second phase (FSP). On the other hand, sample W contained more than 73 % acicular ferrite. The remaining sample W phases were FSP and primary ferrite in approximately equal volume fractions. This data has been assembled in chart form and is shown in Figure (20).

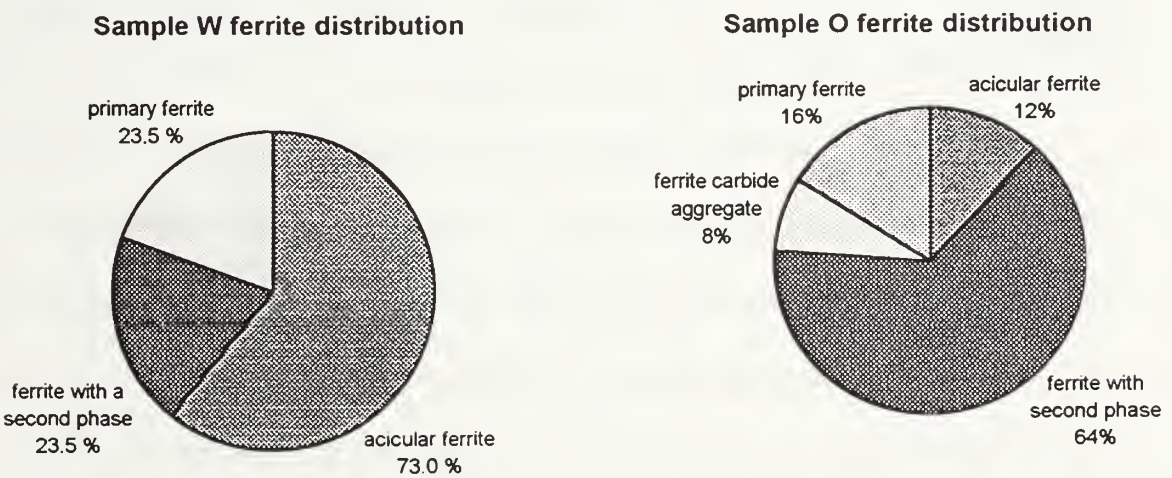

Figure 20 - Pie charts showing the results of quantitative optical microscopy on the two samples W and O

D. INCLUSION SIZE, NUMBER AND VOLUME FRACTION MEASUREMENT

Inclusion size and number measurements were made in the SEM as described in the experimental section and the overall the number of inclusions counted per field were very similar for both samples. Because of the slightly larger average number of inclusions per field in sample W the overall volume percentage was very slightly higher for this sample. These results indicate that the inclusion size and volume fraction are essentially the same for both samples. Table (8) shows the inclusion size and volume fraction data.

Table 8 - Inclusion Distribution within Samples "O" and "W"

	average size in microns	average # inclusion/field	confidence	standard deviation	volume fraction
Sample "O"	0.3056	10.70000	0.00993	0.12619	0.00223
Sample "W"	0.3053	10.90000	0.00799	0.10247	0.00227

The inclusion distributions were analyzed and presented in Figures (21 and 22). The overall mean size and general distribution of both sets inclusions were very similar. The distribution of inclusions is of concern since the larger quantity of small inclusions in the Ti-free sample could have pinned prior austenite grain boundaries possibly reducing the likelihood of acicular ferrite nucleation for reasons other than the absence of Ti.

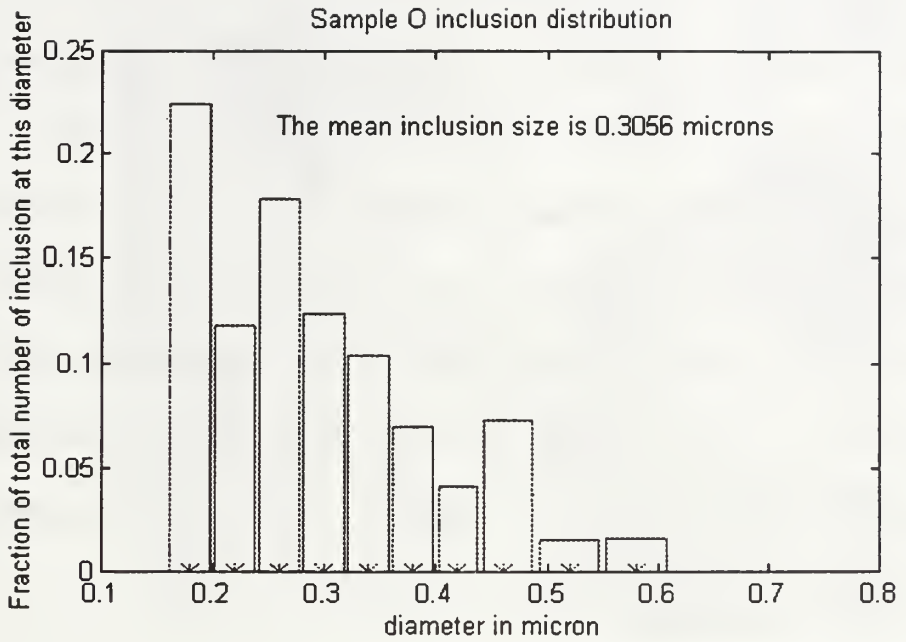

Figure 21 - Inclusion size frequency distribution (Ti-free)

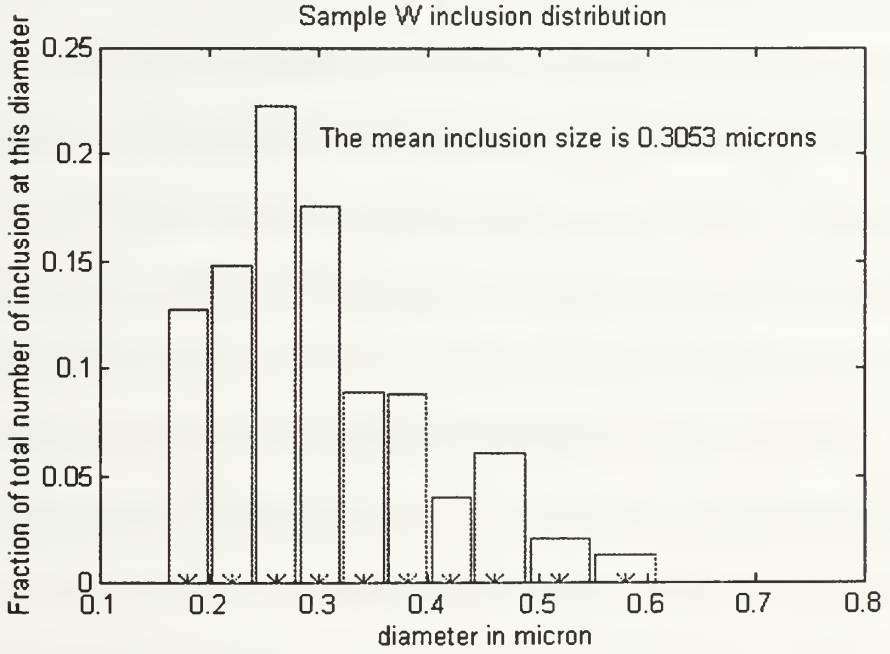

Figure 22- Inclusion size frequency distribution (Ti-rich)

E. TRANSMISSION ELECTRON MICROSCOPY (TEM)

All TEM experiments were performed on a Topcon 002B TEM equipped with a LaB_6 filament using a 200 kV accelerating voltage. Four types of analysis were performed with two different sample preparation techniques. There was some concern that the carbon extraction method would alter later EDX chemical analysis. This was found not to be the case since EDX analysis of inclusions in both electropolished and carbon extraction samples were found to be identical if iron was absent from the inclusion being studied. This indicates that the extraction procedure did not significantly alter inclusion chemistry.

1. TEM Image Analysis

In the Ti-rich sample W acicular ferrite nucleates on inclusions within the austenite matrix. As shown in the following bright field image Figure (23), nucleation is not limited to one platelet, but often consists of several platelets in multiple directions. The formation of one acicular ferrite platelet appears to stimulate the growth of others on the same inclusion [Ref. 10]. This may indicate an autocatalyzing transformation mechanism. Since acicular ferrite is an invariant plane strain transformation, the nucleation of one platelet may set up a strain field that promotes more platelets on the same inclusion to form. This multiple nucleation of platelets is easily seen in Figure (23) where a Ti-rich inclusion has caused the formation of several acicular ferrite platelets.

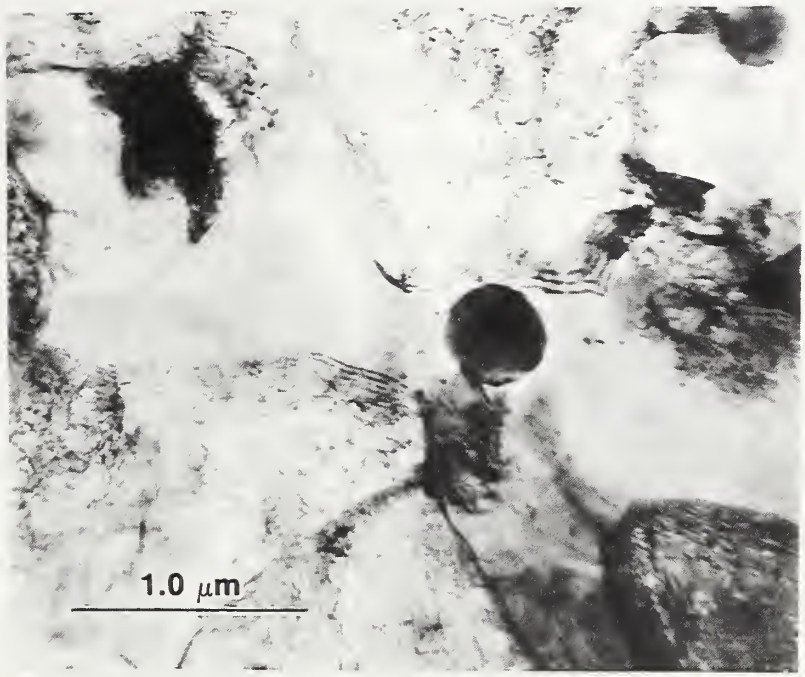

Figure 23 - Micrograph of multiple nucleation of acicular ferrite on a Ti-rich inclusion

2. Electron Diffraction

Electron diffraction was performed on inclusions from both sets of TEM samples. The diffraction pattern, Figure (24), associated with a typical inclusion found in sample O was analyzed and contained interplanar spacings consistent with both the covelite CuS and rhodonite $MnO.SiO_2$ crystal structures. Because of the layered polycrystalline multiphase nature of these inclusions clean diffraction patterns were all but impossible to obtain. The triclinic structure of rhodonite does not exhibit any symmetry and this, together with their polycrystalline nature, makes recognition of low index directions near impossible. Despite this, many of the diffraction spots in Figure (24) were consistent with rhodonite's triclinic structure. Rings from polycrystalline graphite carbon were also clearly visible on the spot

pattern and allowed calibration of the diffraction camera length thus making analysis of the pattern easier. The patterns obtained from the inclusions in the Ti-rich sample W proved even more complex and impossible to analyze with any certainty.

Figure 24 - Electron spot diffraction pattern taken from an inclusion in sample O.

3. EDX and PEELS Analysis of Ti-free Sample O Inclusions

Sample O weld metal deposited using electrodes free of titanium and contained a low acicular ferrite content. Carbon extraction replicas were prepared from sample O to obtain EDX from non-metallic inclusions containing no titanium and which were apparently minimally effective in nucleating acicular ferrite. Standardless oxide analysis

of the EDX data from sample O was difficult due to problems associated with EDX light element analysis. The EDAX software was unable to accurately fit the oxygen K peak using Gaussian profiles and consistently underestimated the oxygen content. Although it was difficult to determine the oxygen content of the inclusions in sample O the EDX analysis for the remaining elements proved to be accurate. In all cases in sample O the inclusions contained Mn and Si with a ratio of 1:1. Occasionally Cu and S were detected, usually with a ratio close to 1:1, suggesting the presence of CuS. PEELS analysis performed on the Ti-free inclusion Figure (25), produced the Mn L_{2-3} and O K edges shown in Figure (26). The ELNES associated with the Mn L_{2-3} edge was compared with the ELNES of the edges obtained from rhodonite by Garvie and Craven [Ref. 37] and excellent agreement for this edge energy (~640 eV) and shape was found.

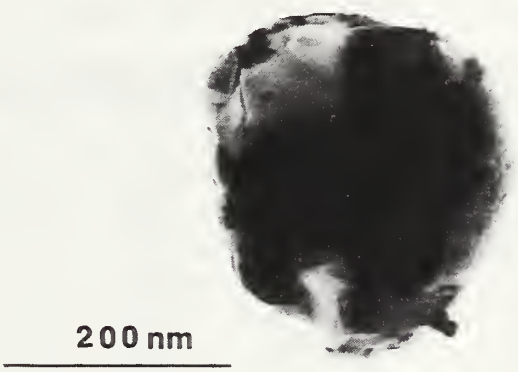

Figure 25 - Bright field TEM micrograph from Ti-free sample O

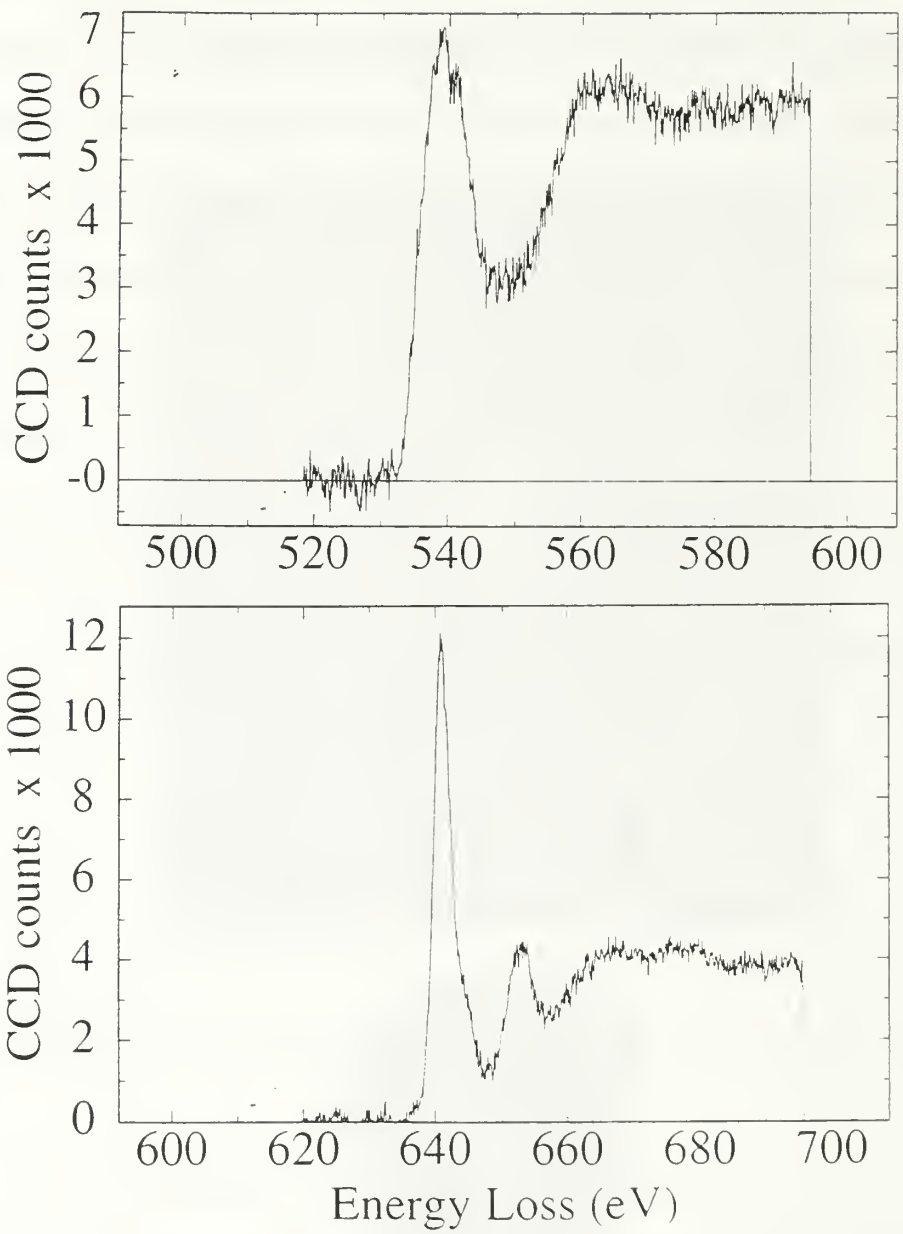

Figure 26 - Mn $L_{2\text{-}3}$ and O K PEELS spectra from the Ti-free inclusion shown in Figure (25).

The electron diffraction experiments also indicated that the phases in these inclusions are $MnO.SiO_2$, rhodonite, and CuS, covelite. This is not surprising , as rhodonite is a very common in inclusion constituent in low Al (<0.005 wt%) steels [Ref. 1,31]. Consequently we can standardize the EDX using the inclusions from sample O and then analyze sample W. In this way an oxygen correction factor may be derived. Several standard inclusions from sample O were analyzed and an average correction factor was calculated as shown in Table (9). The correction factor is the factor by which the measure oxygen concentration must be divided by to obtain the true oxygen concentration in the inclusion.

$$[\text{True Oxygen}] = [\text{Measured Oxygen}] / \text{correction factor} \qquad (12)$$

Since the chemical composition of rhodonite is known an EDX oxygen correction factor can be obtained using the following equation.

$$\text{Correction Factor} = [\text{Measured O}] / \{[\text{Mn}]*1+[\text{Si}]*2\} \qquad (13)$$

Table 9 - Calculation of EDX Oxygen correction factors

Standard Number	Manganese %	Silica %	EDX Oxygen Results %	Correction Factor
1	22.70	23.30	54.00	0.78
2	24.10	23.80	52.10	0.73
3	24.10	24.20	51.30	0.71
4	25.70	25.50	48.80	0.64
5	23.20	23.60	53.10	0.75
6	23.80	23.30	52.80	0.75
7	25.00	25.50	49.50	0.65
8	23.70	23.20	53.10	0.76
9	23.20	23.60	53.20	0.76
10	22.30	23.20	54.50	0.79
Average Oxygen Correction Factor	0.73		Confidence +/-	0.03

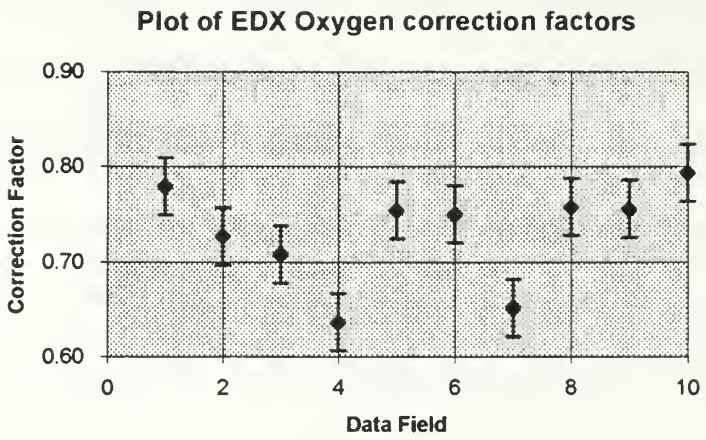

Figure 27 - Plot of EDX correction factors with data confidence error

It should be noted that the carbon layer used to extract the inclusions should be as thin as possible so that the carbon K peak does not interfere with the EDX analysis.

4. EDX and PEELS Analysis of Ti-rich Sample W Inclusions

After EDX analysis of many inclusions near the last weld pass of sample W it was found that these were dominated by two types. Those which appeared to be $MnSiO_3$ together with some titanium and sometimes CuS and those which appeared to be predominately TiO_2 with some iron oxide. An overall EDX analysis of 20 of the inclusions containing $MnSiO_3$ in sample W revealed an average inclusion concentration of Mn 24.1, Si 21.9 and Ti 3.3 (at%). One of these inclusions and its associated EDX spectrum is shown in Figure (28). The phases in these inclusions were generally difficult to separate. However, occasionally, inclusions like the one shown in Figure (29) allowed

small electron probe diameters (~5 nm) to be used to perform high resolution EDX from the different phases.

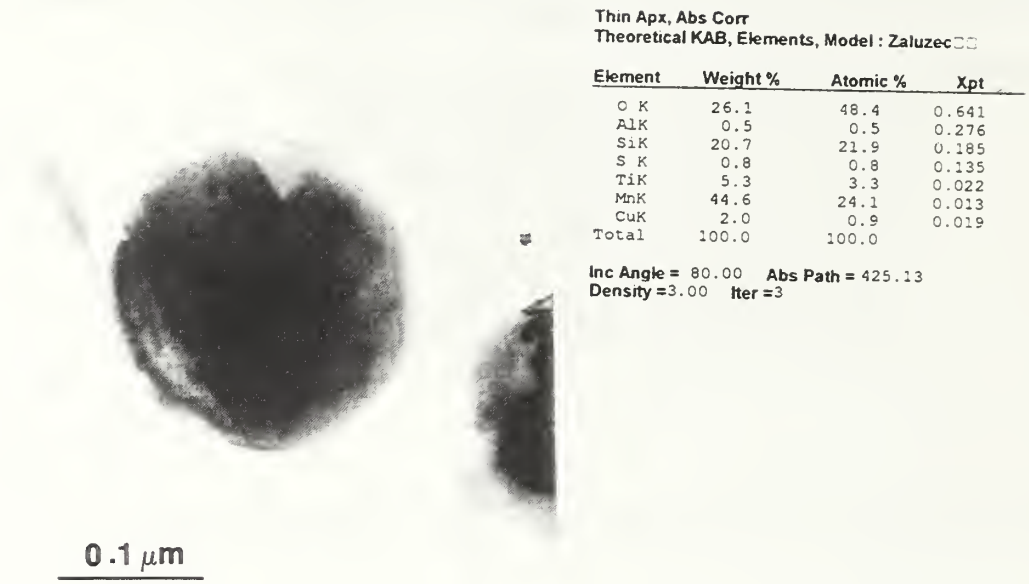

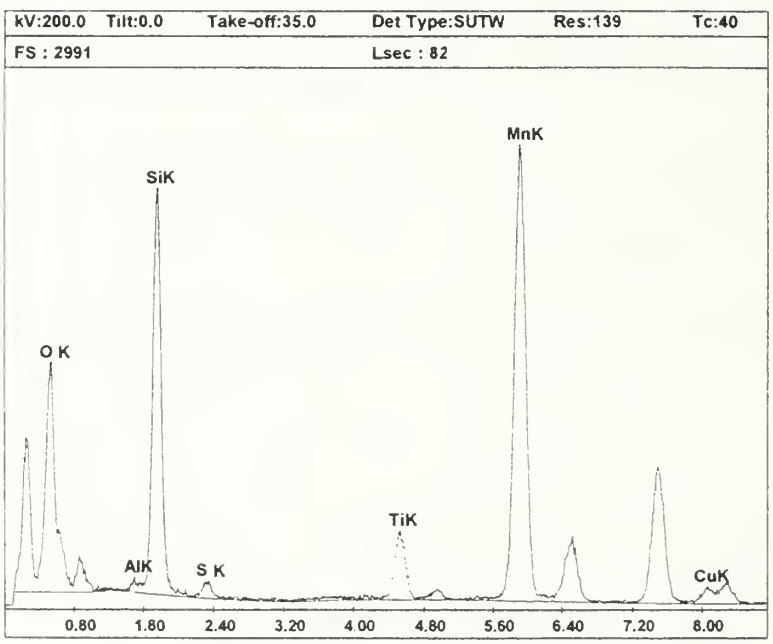

Figure 28 - Typical inclusion from the Ti-rich weldment along with EDX data

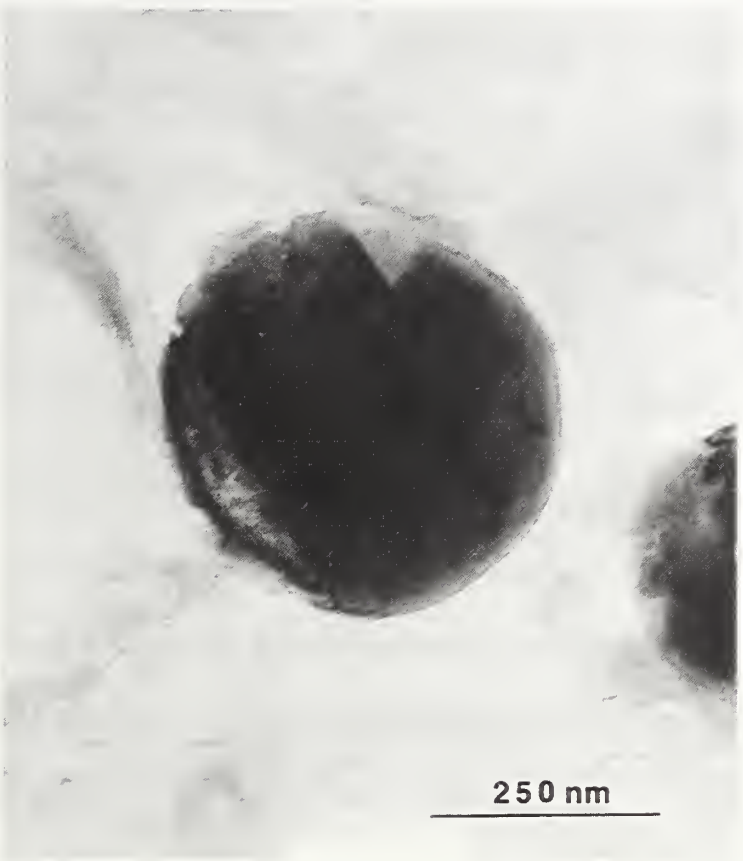

Figure 29 - TEM bright field image of an inclusion from a Ti-rich weld metal

The majority of the inclusion in Figure (29) appears to be rhodonite $MnO.SiO_2$. $MnO.SiO_2$ is not considered an acicular ferrite initiator. It is generally present throughout the inclusion and it exists alone in region (A) from which the EDX spectrum shown in Figure (30) has been taken using a ~5 nm electron probe.

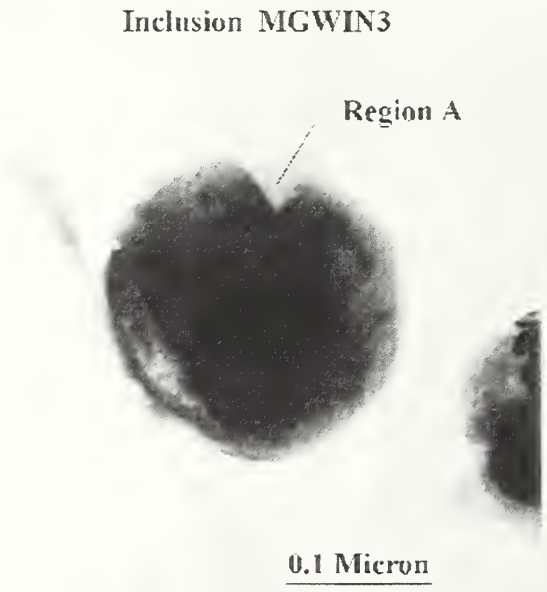

Thin Apx, Abs Corr
Theoretical KAB, Elements, Model : Zaluzec□□

Element	Weight %	Atomic %	Xpt
O K	20.3	39.9	0.055
AlK	0.6	0.6	0.027
SiK	25.0	28.0	0.018
S K	0.6	0.6	0.014
TiK	1.0	0.7	0.002
MnK	51.3	29.4	0.001
CuK	1.3	0.6	0.002
Total	100.0	100.0	

Inc Angle = 80.00 **Abs Path =** 42.51
Density =2.90 **Iter =**2

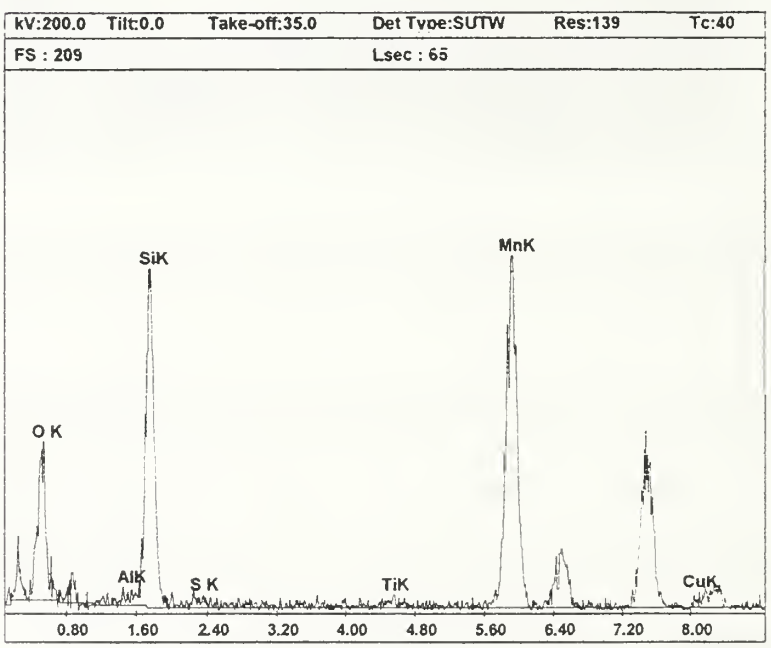

Figure 30 - TEM/EDX analysis of Ti-rich inclusion in Figure (29) showing region (A) which is typical of rhodonite.

Further fine probe analysis of the inclusion in Figure (29) investigated region B near the surface of the inclusion which was composed of primarily Mn, Ti and Si oxides. Note that the summation of the Ti and Si concentrations approximately equals the concentration of Mn in this region. This implies that the Mn in somehow complexed with the Ti here. This may be MnO and TiO_2 in compound form, such as pyrophanite, which has been previously suggested as a component of inclusions responsible for acicular ferrite by Fox et al. [Ref. 31]. The EDX result for the Ti-rich region of the inclusion shown in Figure (29) are presented in Figure (31).

A third phase of interest detected in this inclusion (Figure 29) was copper sulfide, CuS; which was found in region (C) and which also appeared near the edges of inclusions much the same as MnO and TiO_2 phases earlier mentioned. CuS is not an accepted acicular ferrite initiator but its proximity to the inclusion interface is not unexpected since Cu is a strong sulfide former and MnS is less likely to form when the oxygen activity is as high as it is in these SMA weldments. EDX results for region (C) are presented in Figure (32).

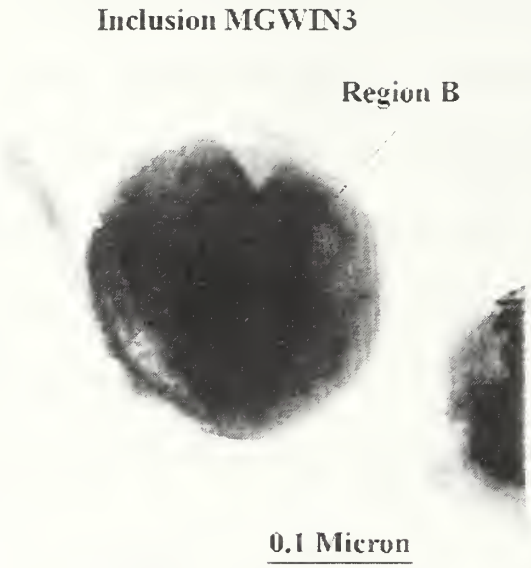

Thin Apx, Abs Corr
Theoretical KAB, Elements, Model : Załuzec□□

Element	Weight %	Atomic %	Xpt
O K	27.7	52.1	1.035
AlK	0.5	0.5	0.355
SiK	13.0	13.9	0.238
S K	0.2	0.2	0.149
TiK	15.3	9.6	0.024
MnK	42.6	23.3	0.021
CuK	0.7	0.3	0.025
Total	100.0	100.0	

Inc Angle = 80.00 Abs Path = 425.13
Density = 3.73 Iter = 4

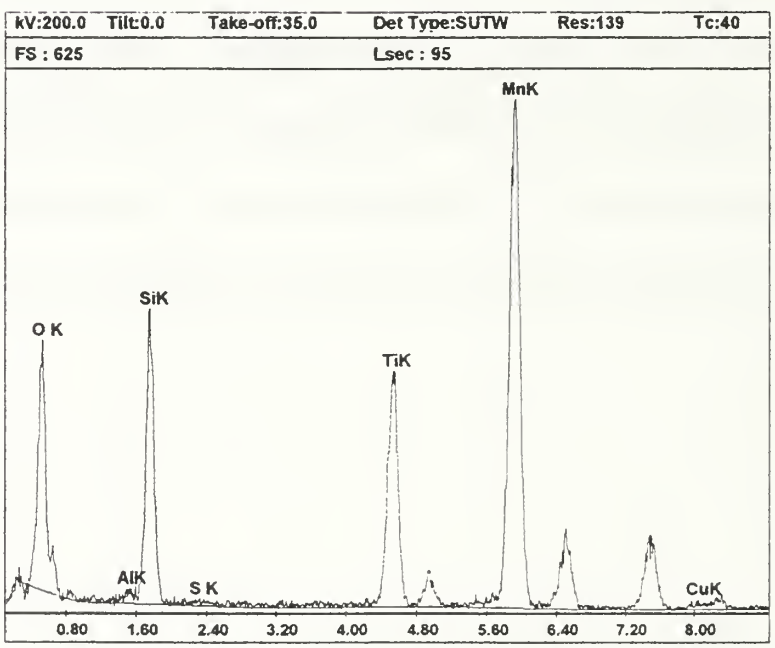

Figure 31 - TEM/EDX analysis of a Ti-rich inclusion showing region (B) rich in a titanium oxide.

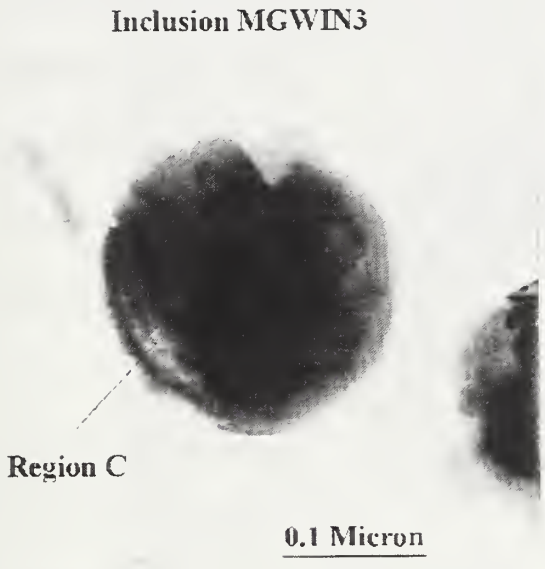

Thin Apx, Abs Corr
Theoretical KAB, Elements, Model : Zaluzec□□

Element	Weight %	Atomic %	Xpt
O K	26.2	49.6	0.828
AlK	0.4	0.5	0.430
SiK	15.0	16.2	0.290
S K	8.3	7.9	0.184
TiK	0.4	0.3	0.036
MnK	26.3	14.5	0.017
CuK	23.3	11.1	0.018
Total	100.0	100.0	

Inc Angle = 80.00 Abs Path = 425.13
Density =4.00 Iter =3

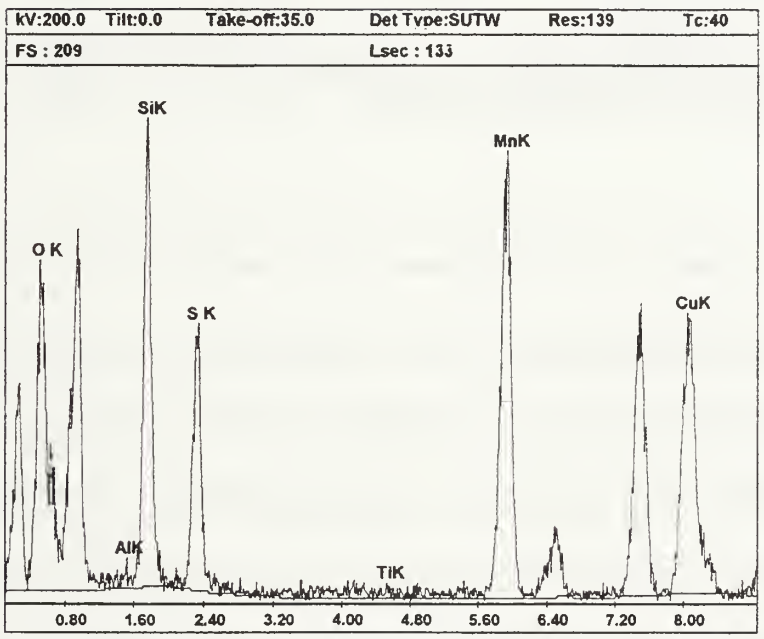

Figure 32 - TEM/EDX analysis of Ti-rich inclusion showing region (C), which is most likely CuS

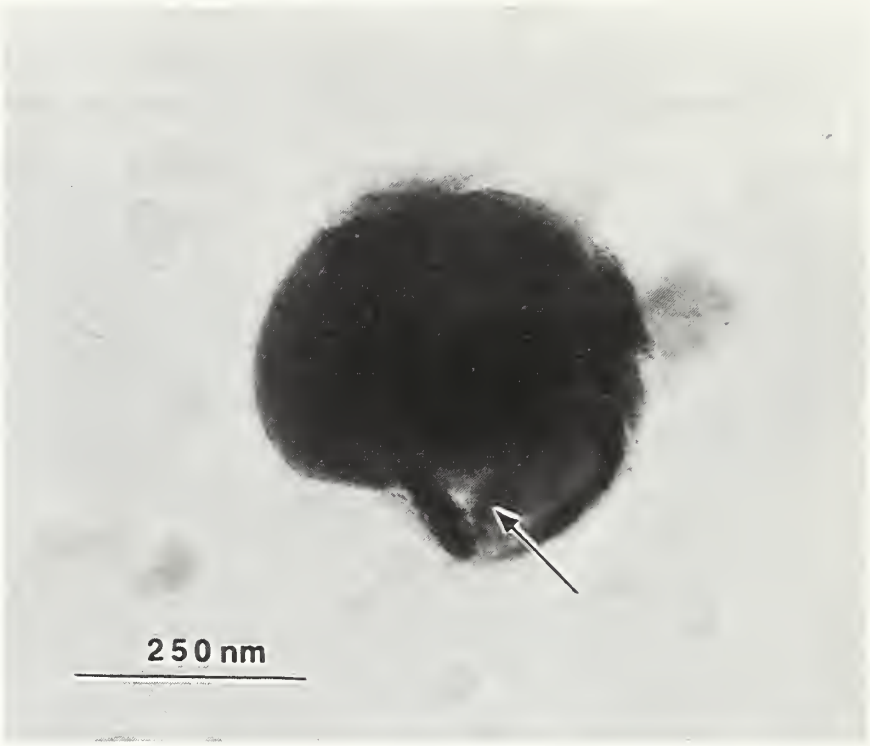

Figure 33 - Ti-rich inclusion with a region (indicated) which is free of Si.

After an extensive search an inclusion with an isolated region containing no Si was found. Its TEM bright field image is shown in Figure (33) with the Si-free region indicated. EDX analysis of the indicated titanium-rich region in the inclusion shown in Figure (33) which contains no silicon, and applying the average oxygen correction factor it was found that Ti is almost certainly present with a valency of four if the valency of Mn is two. By performing a chemical balance on the various oxides contained inside the inclusion, namely Mn and Ti one can postulate oxidation states of each element. Mn normally forms MnO at steel making temperatures [Ref. 32], and MnO_2 would be highly improbable. However, titanium can possibly adopt one of several oxidation states at

steelmaking temperatures [Ref. 22]. Several of these have been reported at these temperatures such as; +2, +3, and +4 that correspond to TiO, Ti_2O_3 and TiO_2 respectively. The sum of these oxides, MnO and Ti_xO_y should add up to the corrected oxygen concentration. If we assume MnO and TiO_2 [Ref. 1,22,31, etc.], the corrected oxygen level matches the calculated one from oxides Table (10).

Table 10 - Oxide correction analysis for the Si-free region of the inclusion shown in Figure (33).

	Measured EDX values	normalized oxides only	assumed oxidation	TiO	TiO_2	Ti_2O_3	Ti_3O_5
Ti	19.20	19.09	+(x) TixO	19.09	38.18	28.64	31.82
Mn	17.40	17.30	+(2) MnO	17.30	17.30	17.30	17.30
Measured O	46.70			36.39	55.48	45.94	49.12
Calculated O	63.97*	57.80	agreement ?	no	yes	no	no

* Calculated using an oxygen correction factor of 0.73.

A PEEL spectrum showing the Ti L_{2-3} edge for a titanium-rich inclusion is shown in Figure (34). Separate standard spectra for two likely titanium oxides are also shown. Figure (34) is arranged with TiO standard (top), TiO_2 standard (middle) and the Ti L_{2-3} and O K spectra from a Ti-rich inclusion at the bottom. The ELNES from Ti L_{2-3} and the O K edges in the inclusion spectrum strongly resembles the Ti L_{2-3} and the O K edges in the uppermost spectrum (TiO) in Figure (34). Note the ~8 eV shift in O K edge energy in TiO_2 that is not present in either the TiO or the inclusion spectra. To eliminate possible

errors the TiO and TiO_2 PEELS spectra were generated by actual analysis of known samples of each that had been pulverized into fine powders which were then placed on Cu grids coated with carbon and analyzed.

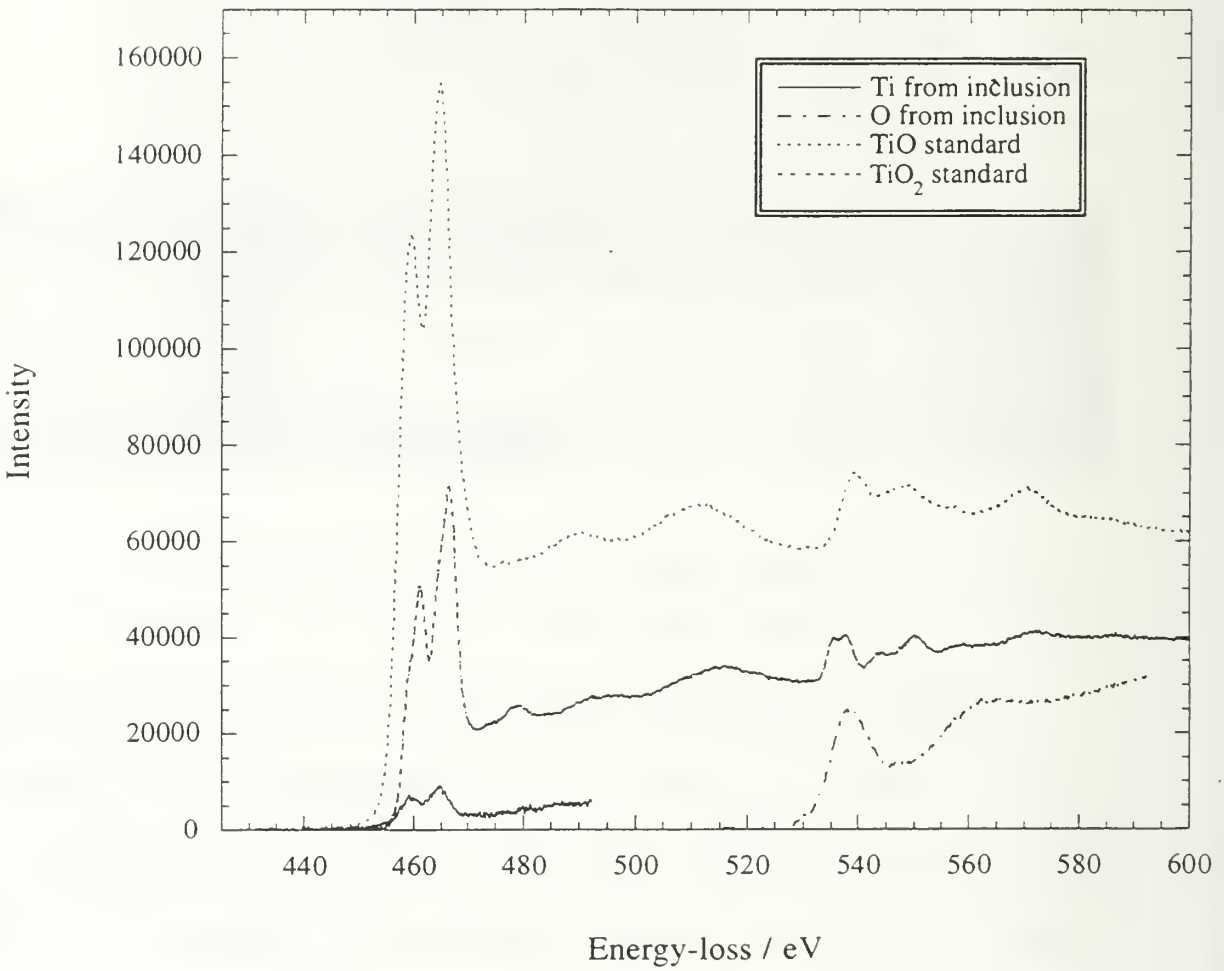

Figure 34 - PEELS spectra for TiO (top), TiO_2 (middle) along with Ti $L_{2,3}$ and O K taken from an inclusion from the Ti-rich sample W (bottom). Note how the oxygen edge energy lines up with the TiO oxygen edge energy.

Both the electron energy loss edge energies and the ELNES from typical Ti-rich inclusions are consistent with a compound exhibiting near-neighbor coordination similar to TiO although it is difficult to discriminate between TiO_2 and TiO using the Ti L_{2-3} edge alone and the ELNES from the O K edge must also contain information concerning the manganese and silicon oxides. Thus, this PEEL spectrum thus neither supports nor contradicts the conclusion that Ti in the Ti-rich inclusions in sample W is in the form of $MnO.TiO_2$ pyrophanite which has been noted before in similar inclusions [Ref. 31] since no PEELS/ELNES information is available at this time for manganese titanate ($MnO.TiO_2$).

Other small inclusions present in the Ti-rich sample W that contained Ti , Fe and Si were also found. These also contained small amounts of Mn and were invariably coated with copper sulfide (CuS). An example of one of these smaller inclusions is shown in Figure (35). On one occasion a small particle which appeared to be $MnO.TiO_2$ was found inside one of these smaller inclusions. It is not likely that these smaller inclusions are responsible for nucleation of acicular ferrite since they are coated with copper sulfide CuS which is present in both the Ti-rich and Ti-free inclusions.

An analysis using PEELS of these smaller inclusions suggests Ti atoms are coordinated in a TiO_2 like fashion. EDX data from these smaller inclusion also suggests TiO_2. This EDX and PEELS data is also shown in Figure (35).

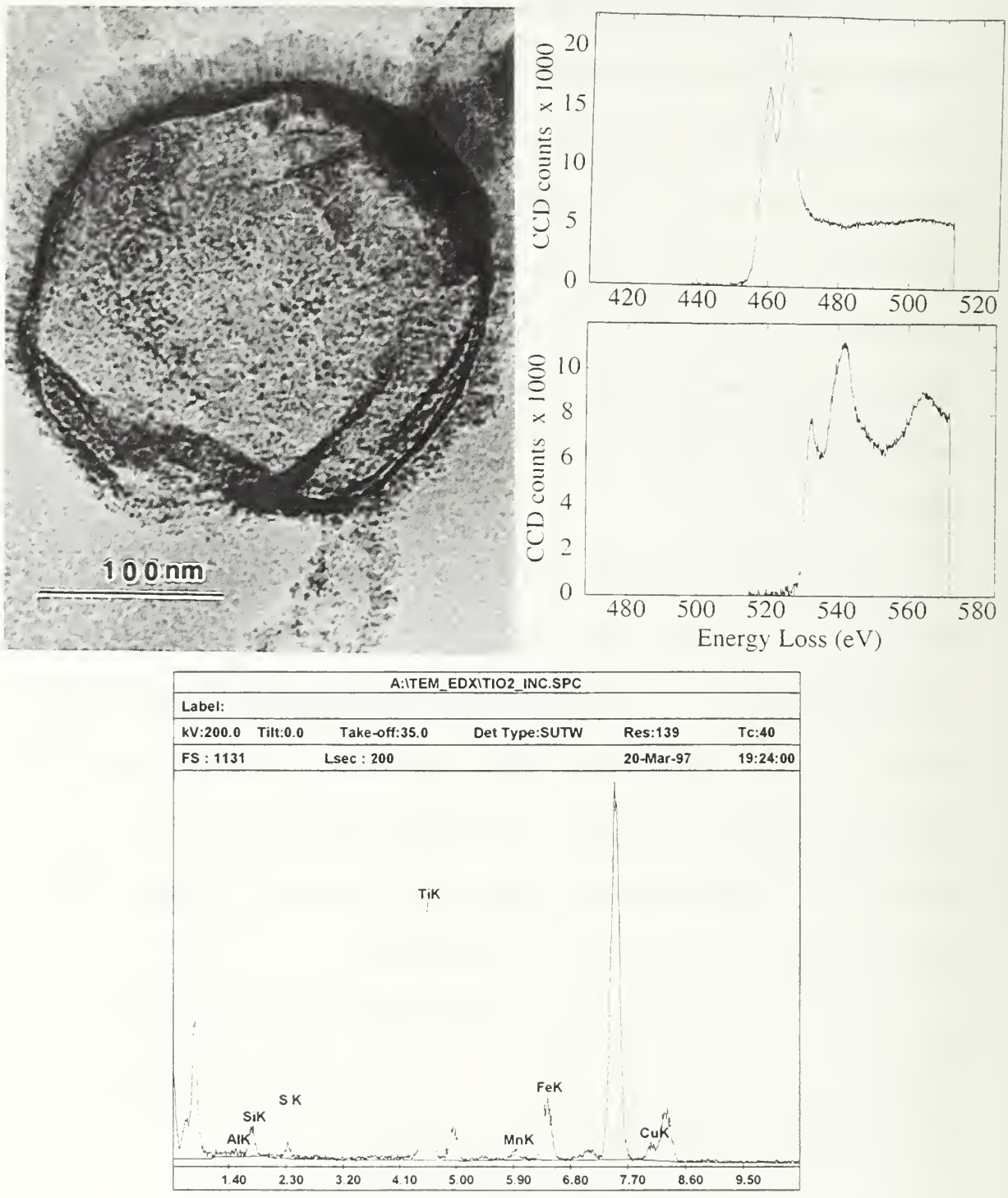

Figure 35 - TEM bright field image of smaller Fe-Ti inclusion found in Ti-rich sample W together with the associated EDX and PEELS spectra.

5. PEELS Elemental Mapping

PEELS elemental maps with spatial resolution of the order of 1 nm were also obtained to show the distribution of Mn, Ti and Si in a typical inclusion from sample W, Figures (36,37,38 respectively). In order to generate these maps the L edges were used for Mn and Ti and the K edge for Si. A gain normalized image is shown in Figure (39) of the inclusion used in PEELS analysis. It is necessary to realize that electron bombardment has altered the shape of this inclusion slightly during the analysis process. The inclusion was approximately round at the start of spectral analysis but as PEELS mapping progressed the inclusion tended toward the shape shown in Figure (39). Figures (36 and 37) are elemental maps generated by developing a background using two measurements prior to the edge energy and then subtracting this background from the signal measured at the edge energy. Figure (38) was made using a jump ratio technique [Ref. 34]. Jump ratio maps are generated by taking a background using one measurement prior to the edge energy and then dividing this background into the measurement taken at the edge energy.

In both mapping techniques the brighter the intensity, the higher the concentration of the particular element. These maps show that the majority of the inclusion has a generally even distribution of both manganese and silicon. However, there are slight variations in this distribution that form areas that appear to have a ratio of less than 1:1 Mn to Si. Figure (36) shows the Mn element map with its evenly distributed concentration of this element. The Ti map is shown in Figure (37). The Ti distribution appears to be slightly more concentrated toward the lower right portion of the inclusion. Silicon appears to be evenly distributed except in the lower right edge of the inclusion,

Figure (38). This is consistent with the conclusion that MnO may be complexed with a titanium oxide in this area instead of SiO_2. This would make the majority of the inclusion $MnO.SiO_2$ rhodonite and a small portion at the lower right edge either MnO mixed with a titanium oxide or possibly $MnO.TiO_2$ pyrophanite.

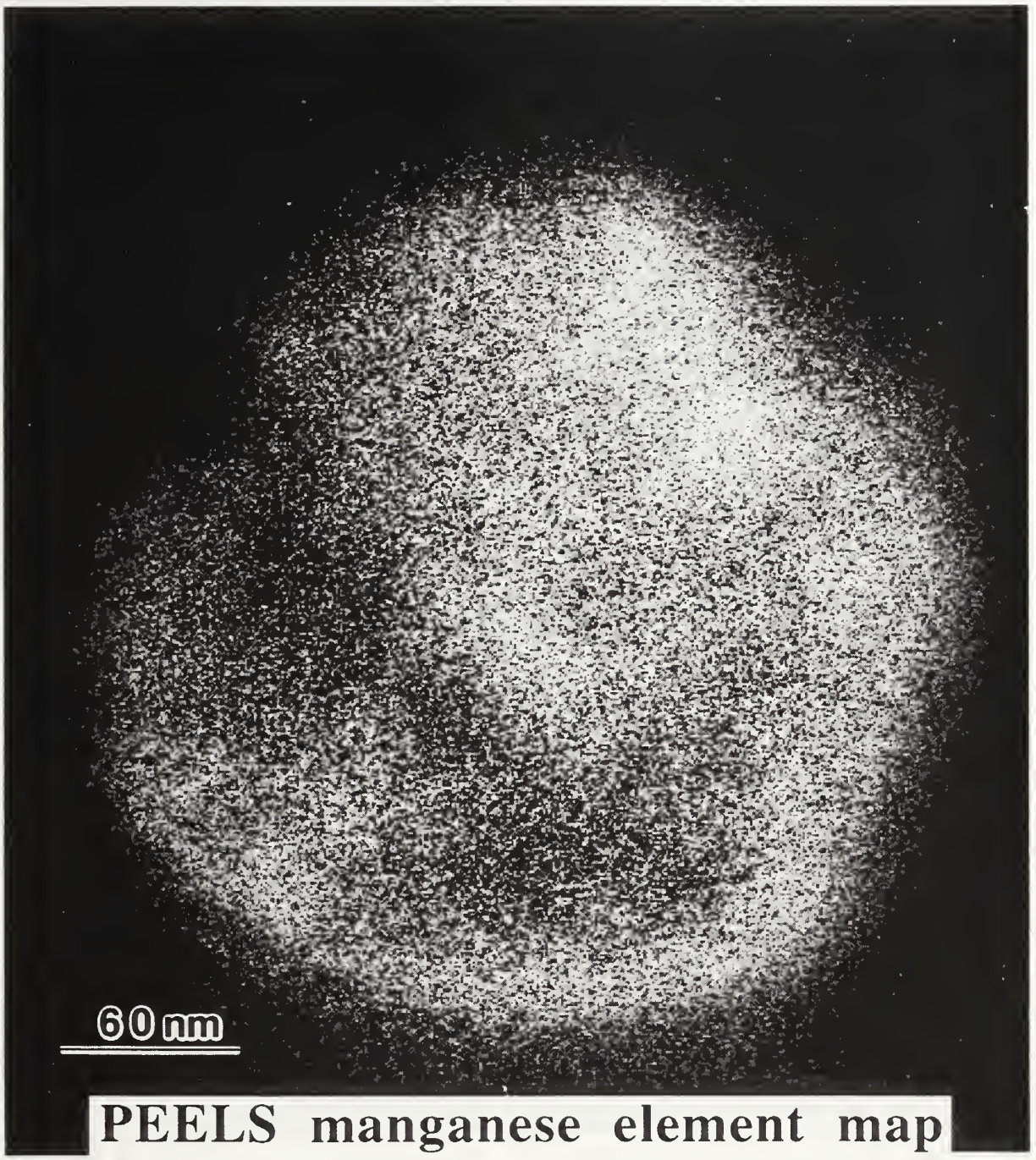

Figure 36 - PEELS elemental map for Mn (L_{2-3} edge) of the Ti-rich inclusion shown in Figure (39).

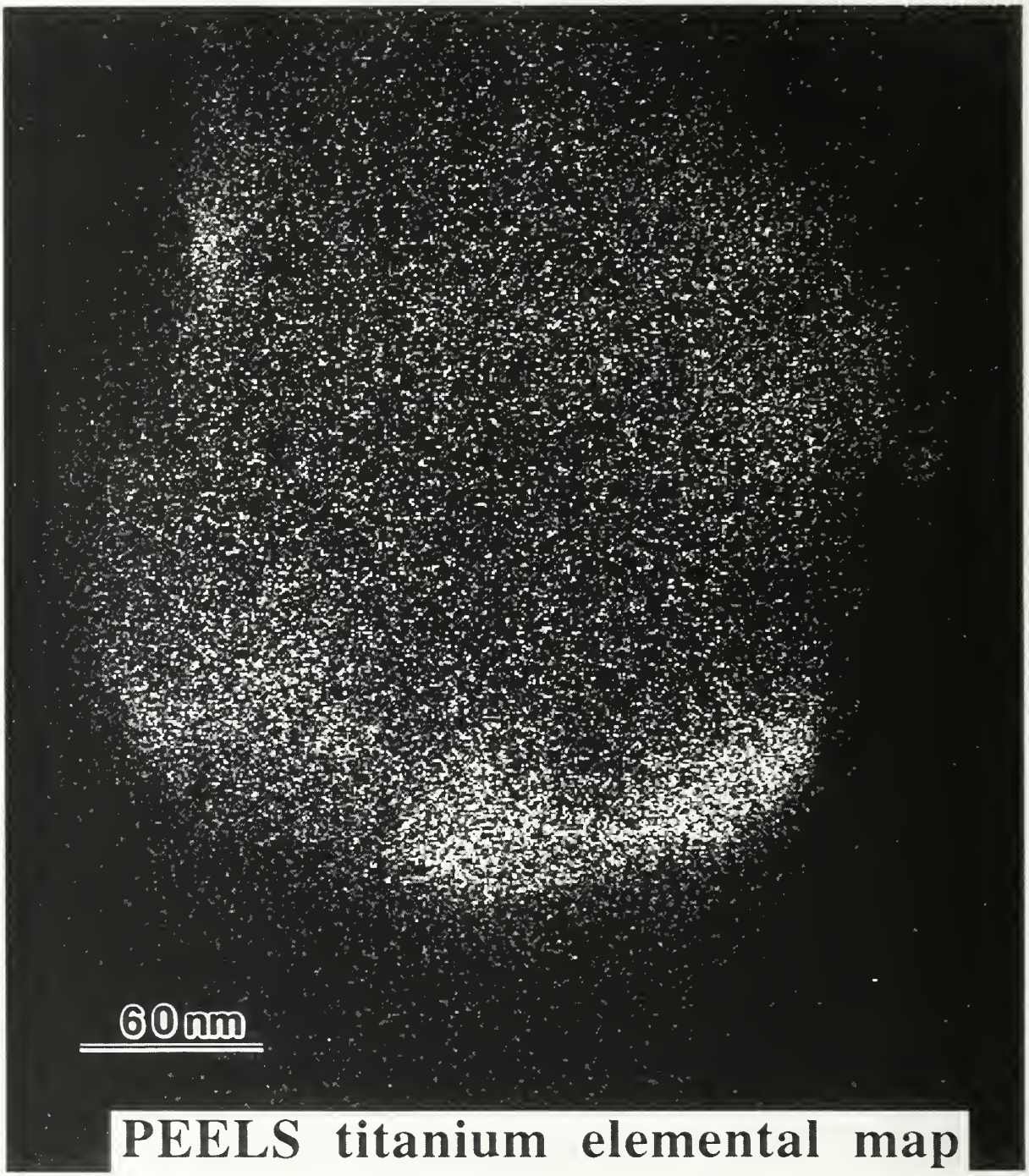

Figure 37 - PEELS elemental map for Ti ($L_{2\text{-}3}$ edge) of the Ti-rich inclusion shown in Figure (39).

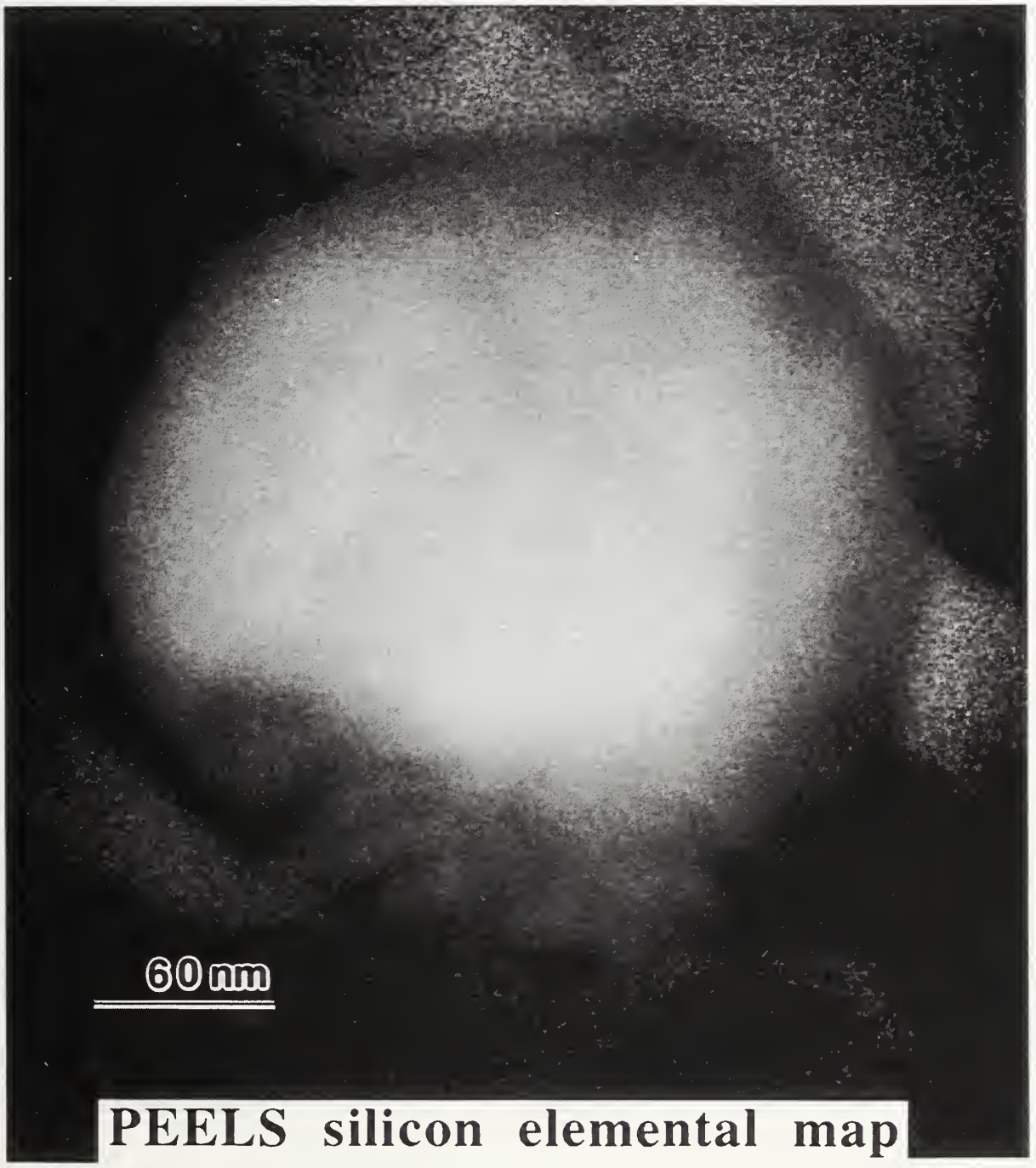

Figure 38 - PEELS Si (K) jump ratio map taken from the Ti-rich inclusion shown in Figure (39).

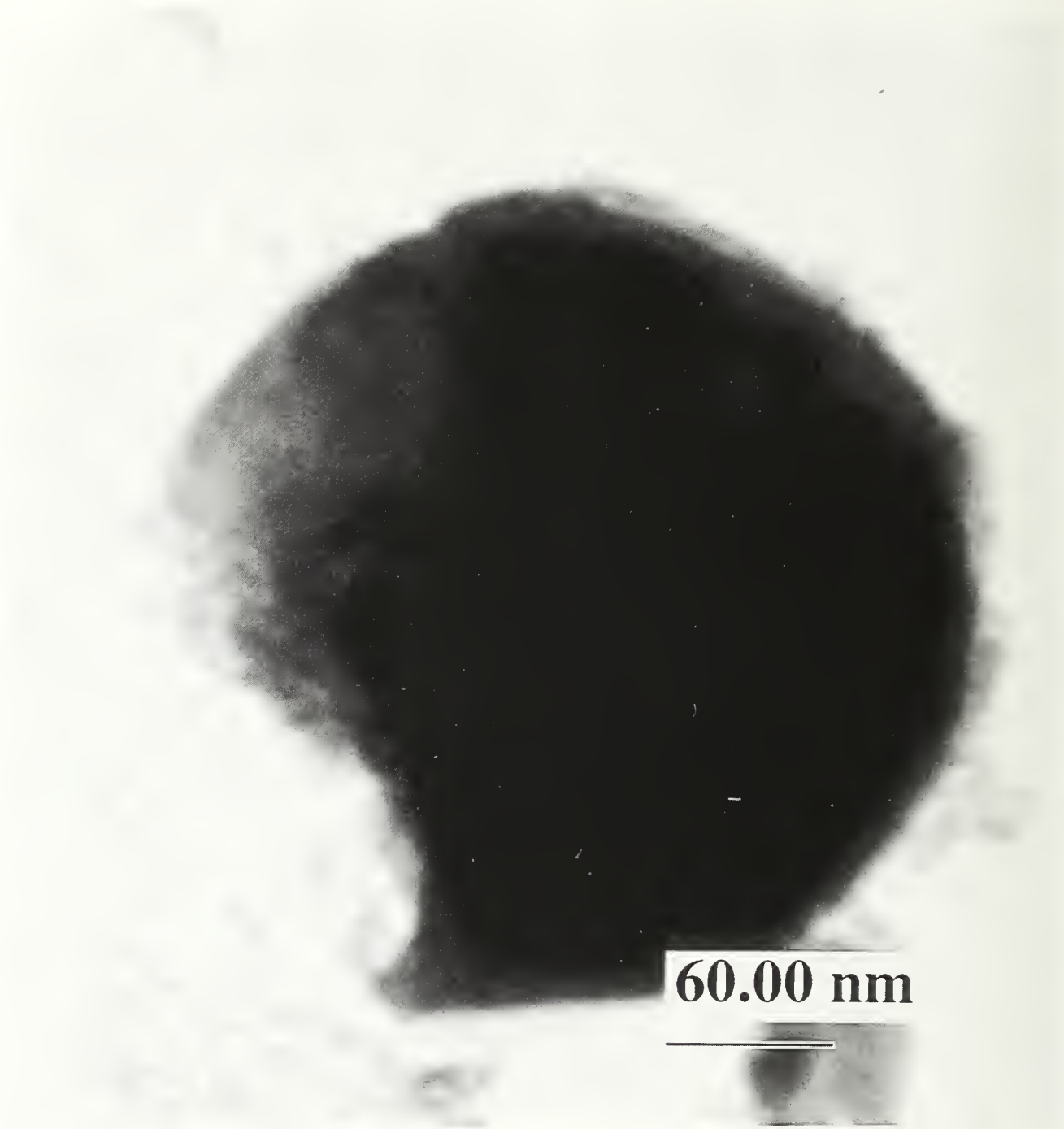

Figure 39 - TEM/PEELS gain normalized image of a Ti-rich inclusion, the subject of the elemental maps shown in Figures (36-38).

It does appear that most Ti and Mn rich regions are evenly dispersed over the surface of the inclusion with the exception of the lower right edge. Whether a titanium oxide is complexed with MnO or it exists alone, it is logical to conclude that either $MnO.TiO_2$ or a titanium oxide alone caused the acicular ferrite nucleation seen in sample W.

6. Pyrophanite

From the $MnO\text{-}TiO_2$ phase diagram Figure (40) we see that pyrophanite, $MnO.TiO_2$, remains as a liquid as low as 1360 °C. This low temperature oxygen-rich molten compound at the surface of inclusions could possibly react with alloy elements in the matrix in the local vicinity of the inclusion. If these inclusions leach Mn and C from the local matrix while reducing small amounts of TiO_2 to TiO [Ref. 10] this would make the surrounding steel less hardenable, thus allowing acicular ferrite to form more easily. At the very least, the solidification of such compounds at the interface between two solid interfaces may cause a strain field which could be linked to acicular ferrite formation as stated in [Ref. 10]. It does not seem that simple epitaxial growth of acicular ferrite from pyrophanite is likely because there does not appear to be any planes in the latter that can register in a simple fashion with the α-ferrite.

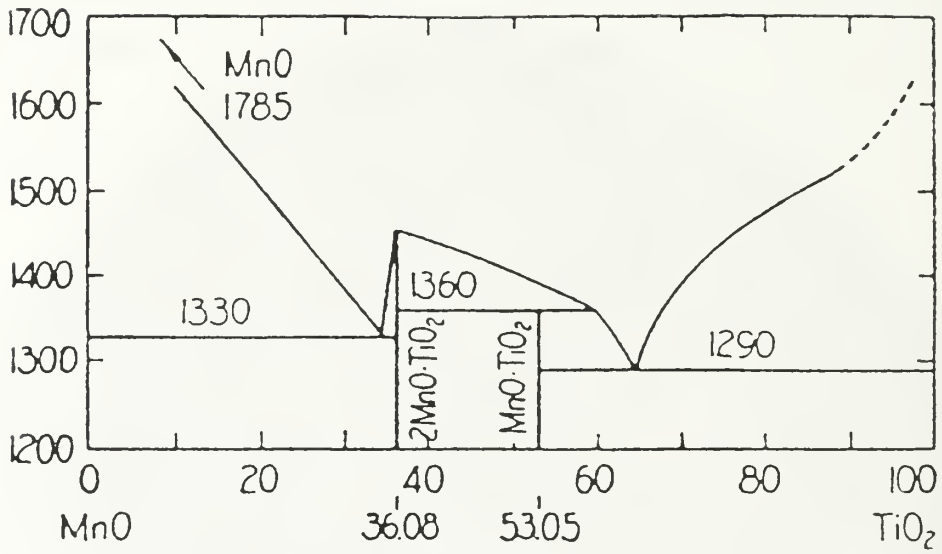

Figure 40 - MnO-TiO_2 phase diagram.

V. SUMMARY

A. CONCLUSIONS

For the C-Mn steel weld metal studied in the present work, 28 ppm titanium is sufficient to raise the acicular ferrite concentration in these steels to 73%, giving very impressive "as-welded" strength and toughness (100 J Charpy fixed energy temperature of -88 °C).

It is unnecessary to perform post weld heat treatments when using welding electrodes of the composition indicated in the present work. As welded mechanical properties are as strong and tough as any that were attained through post weld heat treatment outlined here.

A titanium oxide was found in the inclusions that appeared to cause acicular ferrite to nucleate. Mn was almost always present the titanium oxides indicating the possible presence of a manganese titanate $MnO.TiO_2$ called pyrophanite. The existence of both TiO and TiO_2 within weld metal inclusions may indicate a reduction reaction that possibly lowers local alloy concentrations in the vicinity of the inclusions. Despite the extensive investigation of the titanium oxides present in the inclusions in sample W the mechanism by which these inclusions nucleate acicular ferrite is still a mystery.

B. SUGGESTIONS FOR FURTHER STUDY

PEELS analysis should be performed on pyrophanite so that the spectra from this mineral can be compared with the results of the present work.

A study of the coordination of Ti in pyrophanite could provide information which might confirm that Ti is present as $MnO.TiO_2$ in these Ti-rich inclusions.

New methods to obtain thin inclusion samples for TEM work need to be devised. Current sample preparation technology does not allow for thinning of fine hard particles in a relatively soft matrix.

A study into the strain field effects experienced by the steel matrix when a spherical inclusion embedded the steel experiences thermal stress. A finite element/difference model may be useful in modeling these stress fields. Comparison of the model's results and experimental results that have been conducted by Bhadeshia [Ref. 10] may shed light on the nature of misfit strain and its relationship to inclusion nucleated acicular ferrite.

A notable deficiency in current research is hot stage TEM observation of the acicular ferrite nucleation process. To the author's knowledge no one, as yet, has directly observed the formation of an acicular platelet on an inclusion. This direct observation may give insight into aspects such as autocatalysing nucleation that appears to occur in many TEM images.

A Scanning Auger Electron Spectroscopy investigation of the local alloy concentration in the weld metal region surrounding the inclusions and the inclusions themselves could provide useful information. By sputtering off layers of the sample

surface with argon ions a concentration profile may be obtained of alloying elements such as carbon and manganese in and around the inclusions. Mn and C elements that are thought to be depleted locally around the inclusions increasing the likelihood of acicular ferrite nucleation.

REFERENCES

1. Fox, A.G. and Brothers, D.G., 1995. The role of titanium in the non-metallic inclusions which nucleate acicular ferrite in the submerge arc weld (SAW) fusion zones of Navy HY100 steel. Scripta Metallurgica et Material 32 (7):1061-1066.
2. Egerton, R. F., 2nd Edition, 1996. Electron Energy-Loss Spectroscopy in the Electron Microscope.
3. Gregg, J. M. and Bhadeshia, H. K. D. H., Solid-State Nucleation of Acicular Ferrite on Minerals added to Molten Steel; Acta Metallurgica, Inc., Vol 45, No. 2, 1997, pg 739-748.
4. Evans, G. M., Microstructures and Properties of Ferritic Steel Welds Containing Ti and B Doc II-A-932-94.
5. Babu, S. S. and Bhadeshia, H. K. D. H., Mechanism of the Transition from Bainite to Acicular Ferrite; Reprinted from Materials Transactions, Jim, Vol. 32 No. 8, August 1991 pg 679-688.
6. Grong, O., Kluken, A. O., Nylund, H.K., Dons, A.L. and Hjelen, J., Catalyst Effects in Heterogeneous Nucleation of Acicular Ferrite; Metallurgical and Materials Transition A, Vol. 26A, March 1995, pg 525-534.
7. DeHoff, R. T. and Rhines, F. N., Quantitative Microscopy; McGraw-Hill, Inc.1996 pg46-48,54,60.

8. Yang, J. R. and Bhadeshia, H. K. D. H., Orientation Relationships Between Adjacent Plates of Acicular Ferrite in Steel Weld Deposits Materials Science and Technology, January 1989, Vol. 5 pg 93-97.

9. Babu, S. S. and Bhadeshia, H. K. D. H., Stress and the Acicular Ferrite Transformation Materials Science and Engineering, A156 (1992) pg 1-9.

10. Bhadeshia, H. K. D. H., Bainite in Steels The Institute of Materials, 1992 pg 245-282

11. Evans, G. M., Effect of Nitrogen on C - Mn Steel Welds Containing Titanium and Boron; AWS Show 1995, pg 1-13, Tables 1-3, Figures 1-19.

12. Evans, G. M., Microstructure and Properties of Ferritic Steel Welds Containing Al and B.

13. Dowling, J.M., Corbett, J.M. and Kerr, H.W., 1986. Observations on inclusions and acicular ferrite nucleation in submerged are HSLA welds in high strength low alloy steels.

14. Fleck, N.A., Grong O., Edwards, G. R. and Matlock, D. K., 1986. The role of filler metal wire and flux composition in submerged arc weld metal transformation kinetics. Welding Journal 65(5): 113-s to 121-s.

15. Thewlis, G., 1986. The influence of pipe plate and consumable chemistry on the composition, microstructure and toughness of weld metal. Proceedings of Welding and Performance of Pipelines Conference, Paper 9, The Welding Institute, Abington, U.K.

16. Abson, D. J., 1987. Small Particles in Weld Metals - A Review. International Institute for Welding Document IXJ-122-87.

17. Lau, T.W., Sadowsky, M.M., North, T.H. and Weatherly, C.G., 1987. Effect of nitrogen on the toughness of HSLA weld deposits. Proceedings of an International Conference on the Welding Metallurgy of Structural Steels, pp. 349-3654, The Metallurgical Society, Warrendale, Pa.

18. Chijiiwa, R., Tamehiro, H., Hirai, H., Matsuda, H. and Mirmura, H., 1988. Proceedings of a Conference on Offshore Mechanics and Arctic Engineering, pp. 1-8.

19. Lau, T.W., Sadowsky, M. M., North, T. H. and Weatherly, C. G., 1987. Effect of nitrogen on the toughness of HSLA weld deposits. Materials Science and Technology 4: 52-61.

20. Kluken, A.O. and Grong, O., 1989. Mechanisms of inclusion formation in Al-Ti-Si-Mn deoxidized steel weld metals. Metallurgical Transactions A 20:1335-1349.

21. Evans, G.M., 1992. The effect of titanium in SMA C-Mn steel multipass deposits. Welding Journal 71(12):447-s to 454-s.

22. Babu, S.S., David, S.A., Vitek, J.M., Kundra,K. and DebRoy, T., 1995. Development of macro- and microstructures of C-Mn low alloy steel welds - inclusion formation. Materials science and Technology 11:186-199.

23. Goodhew, P.J. and Humphreys, F.J., 2nd Edition, 1988. Electron Microscopy and Analysis.

24. Ricks, R.A., Howell, P.R. and Barrite, G.S., 1982. The nature of acicular ferrite in HSLA steel weld metals. Journal of Materials Science, 17:732-740.

25. Barrite, G.S. and Edmonds, D.V., 1981. The microstructure and toughness of HSLA steel weld metals. Proceedings on Advances in the Physical Metallurgy of Steels Conference, pp. 126-135, The Metals Society.

26. Yamamoto, K., Matsuda, S., Haze, T., Chijiiwa, R. and Mimura, H., 1987. Proceedings of a conference on Residual and Unspecified Elements in Steel, pp. 1-24, ASM International, Materials Park, Ohio.

27. Harrison, P.L. and Farrar, R.A., 1981. Influence of oxygen-rich inclusions on the austenite-to-ferrite phase transformations in high-strength-low-alloy (HSLA) steel weld metals. Journal of Materials Science 16:2218-2226.

28. Sugden, A.A.B. and Bhadeshia, H.K.D.H., 1988. The non uniform distribution of inclusions in low-alloy steel weld deposits. Metallurgical Transactions A 19:669-674.

29. Horii, Y., Wakabayashi, M., Okhita, S. and Namura, M., 1988. Study of the Toughness of Large Heat Input Weld Metal for Low Temperature Service TMCP Steel. Nippon Steel Technical Report No. 37, pp. 1-9, the Nippon Steel Co., Japan.

30. Ringer, S. R., Barbaro, F., Krauklis, P. and Easterling, K., 1990. Proceedings of a Conference on Microstructure Control to Achieve Properties in Modern Steels. Pp. 1-6, Institute of Metals and Materials, Australasia, Melbourne.

31. Fox, A. G., Eakes, M. W. and Frank, G. L., 1996. The Effect of Small Changes in Flux Basicity on the Acicular Ferrite Content and Mechanical Properties of Submerged Arc Weld Metal of Navy HY-100 Steel. Welding Journal 75(10):330-s to 342-s.

32. Kiessling, R. and Lange, N., 1978. Non-Metallic Inclusions in Steel. The Metals Society.

33. Cerjak, H., Letofsky, E. , Pitoiset, X., Seiringer, A., 1995. The Influence of the Microstructure on the Toughness of C-Mn Multi-Run-Weld Metals. IIW-Doc IX-1814-95.

34. Williams, D. B., Carter, C. B., 1996. Transmission Electron Microscopy, Spectroscopy, Vol. IV. Plenun Publishing Corp.

35. Microstructural Identification Methods and Techniques. 1985. 1D1, 11W-DOC No. 1XJ-102-85

36. Ahn, C. C. and Krivanek, O. L., 1983. A Reference Guide of Electron Energy Loss Spectra Covering all Stable Elements, EELS Atlas, Gatan Inc.

37. Gravie, L. A. J., Craven, A. J., 1994. High-resolution Parallel Electron Energy-loss Spectroscopy of Mn $L_{2,3}$ -Edges in Inorganic Manganese Compounds. Physics and Chemistry of Minerals 21:191-206.

INITIAL DISTRIBUTION LIST

1. Defense Technical Information Center 2
   8725 John J. Kingman Road., Ste 0944
   Ft. Belvoir, VA 22060-6218

2. Dudley Knox Library 2
   Naval Postgraduate School
   411 Dyer Rd.
   Monterey, CA 93943-5101

3. Naval Engineering Curricular Office (Code 34) 1
   Naval Postgraduate School
   Monterey, CA 93943-5000

4. Department Chairman, Code ME 1
   Department of Mechanical Engineering
   Naval Postgraduate School
   Monterey, CA 93943-5000

5. Dr. Alan G. Fox, Code ME/KX 2
   Department of Mechanical Engineering
   Naval Postgraduate School
   Monterey, CA 93943-5000

6. Mr. Joe Blackburne 1
   Naval Surface Warfare Center
   Carderock Division, Code 615
   9500 McAurthur Boulevard
   Bethesda, Maryland 20084-5000

7. Dr. G. M. Evans..... 1
   The Welding Institute.
   Abington Hall
   Abington, Cambridge CB1 A6L United Kingdom

8. Lt. Michael K. Greene..... 2
   8460 Woodbury Rd.
   Laingsburg, MI 48848